Asymmetrical localization of Nup107-160 subcomplex components within the nuclear pore complex in fission yeast

*Haruhiko Asakawa[1], Tomoko Kojidani[2,3], Hui-Ju Yang[1], Chizuru Ohtsuki[1], Hiroko Osakada[2], Atsushi Matsuda[2], Masaaki Iwamoto[2], Yuji Chikashige[2], Naomi Takagi[4], Koji Nagao[4,5], Chikashi Obuse[4,5], *Yasushi Hiraoka[1,2] & *Tokuko Haraguchi[1,2]

1 Graduate School of Frontier Biosciences, Osaka University, Suita, Japan

2 Advanced ICT Research Institute Kobe, National Institute of Information and Communications Technology, Kobe, Japan

3 Department of Chemical and Biological Sciences, Faculty of Science, Japan Women's University, Tokyo, Japan

4 Graduate School of Life Science, Hokkaido University, Sapporo, Japan.

5 Graduate School of Science, Osaka University, Toyonaka, Japan.

*Corresponding authors:

Tokuko Haraguchi

e-mail: tokuko@nict.go.jp

Yasushi Hiraoka

e-mail: hiraoka@fbs.osaka-u.ac.jp

Haruhiko Asakawa

e-mail: askw@fbs.osaka-u.ac.jp

Abstract

The nuclear pore complex (NPC) forms a gateway for nucleocytoplasmic transport. Nup107-160 subcomplexes, key components for building the NPC, are believed to be symmetrically localized on the nuclear and cytoplasmic sides of the NPC. However, in *S. pombe*, immunoelectron microscopic and genetic interaction analyses revealed that the Nup107-160 subcomplexes had an asymmetrical localization: constituent proteins spNup131, spNup120, spNup85, spNup96, spNup37, spEly5, and spSeh1 were localized on the cytoplasmic side whereas spNup132 and spNup107 were on the nuclear side, suggesting the complex was split into two pieces in *S. pombe*. The expression of a fusion protein of spNup96 with spNup107 caused cytoplasmic relocalization of spNup107. In this strain, half of the spNup132 proteins changed their localization to the cytoplasmic side of the NPC, leading to defects in mitotic and meiotic progression. These observations suggest the asymmetrical structure of the Nup107-160 subcomplex in fission yeast is necessary for normal cell cycle progression.

Keywords: nuclear pore complex, nucleoporin, Nup133, Y-complex, immunoelectron microscopy

Introduction

In eukaryotes, the nuclear envelope (NE) separates the nucleus from the cytoplasm. Molecular transport between the nucleus and cytoplasm across the NE occurs through nuclear pore complexes (NPCs). These complexes are cylindrical, eight-fold symmetrical structures that perforate the NE and are made of multiple sets of about 30 different protein species known as nucleoporins (Nups) (Rout et al., 2000; Cronshaw et al., 2002; Alber et al., 2007). Nups are classified into three groups: transmembrane Nups, FG repeat Nups, and scaffold Nups. Transmembrane Nups have transmembrane helices and anchor NPCs to the NE. FG repeat Nups contain phenylalanine-glycine (FG) rich repeats and are involved in molecular transport through the NPC cylinder structure. Scaffold Nups form two inner rings and two outer rings, which serve as the NPC structural core (Bui et al., 2013; von Appen et al., 2015; Kosinski et al., 2016; Lin et al., 2016), and associate with the membrane through interactions with transmembrane Nups (Alber et al., 2007; Onischenko et al., 2009; Eisenhardt et al., 2014). These NPC structures and most Nups are generally conserved among eukaryotes (Rout et al., 2000; Cronshaw et al., 2002; DeGrasse et al., 2009; Tamura et al., 2010; Amlacher et al., 2011; Obado et al., 2016a), although numerous species-dependent differences are found (Knockenhauer and Schwartz, 2016).

The Nup107-160 subcomplex is a key component of the outer rings and in most eukaryotes is composed of equal numbers of Nup107, Nup85, Nup96, Nup160, Nup133, Sec13, and Seh1, and depending on the species Nup37, Nup43, and ELYS are also included (Walther et al., 2003; Harel et al., 2003; Loïodice et al., 2004; Rasala et al., 2006; Liu et al., 2009; Thierbach et al., 2013). These Nups assemble to form, both *in vitro* and *in vivo*, the Y-shaped Nup107-160 subcomplex in *Homo sapiens*, the budding

70 yeast *Saccharomyces cerevisiae,* and the thermophile *Chaetomium thermophilum* (von
71 Appen et al., 2015; Thierbach et al., 2013; Kampmann and Blobel, 2009; Flemming et
72 al., 2010; Fernandez-Martinez et al., 2012; Kelley et al., 2015; Stuwe et al., 2015).
73 Nup85, Nup43, and Seh1 form one of the two short arms, while Nup160, Nup37, and
74 ELYS form the other. The two arms are connected to Nup96 and Sec13, and Nup96 is
75 connected to Nup107 and Nup133 to form the long stem (Nup96-Nup107-Nup133) of
76 the Y-shaped molecule. Multiple copies of the Nup107-160 subcomplex form the outer
77 rings on the nucleoplasmic and cytoplasmic sides of the NPC (Bui et al., 2013; von
78 Appen et al., 2015; Stuwe et al., 2015; Kim et al., 2018).
79 Like other eukaryotes, the fission yeast *Schizosaccharomyces pombe* has a set of
80 conserved Nups (Baï et al., 2004; Chen et al., 2004; Asakawa et al., 2014) (hereafter, we
81 use ‘sp’ to denote *S. pombe* proteins and 'sc' and 'hs' to indicate *S. cerevisiae* and *H.*
82 *sapiens* proteins). However, the *S. pombe* NPC has several unique features. It contains
83 spEly5 (a potential homolog of metazoan ELYS) and spNup37, but lacks Sec13 and
84 Nup43 (Asakawa et al., 2014), and it has two redundant Nup133 homologs (spNup131
85 and spNup132) in addition to two redundant scNic96/hsNup93 homologs (spNpp106
86 and spNup97). Most strikingly, the Nup107-160 subcomplex in *S. pombe* is composed
87 of unequal numbers of spNup107, spNup120 (a homolog of hsNup160), spNup85,
88 spNup96, spNup37, spEly5, spSeh1, spNup131 and spNup132 (Asakawa et al., 2014);
89 the relative numbers of spNup107and spNup131 are 4 - 8 in a single NPC, and that of
90 spNup132 is approximately 48 whereas the other components are approximately16.
91 Thus, a unique/different structural organization of the Nup107-160 subcomplex is
92 suggested in *S. pombe* compared with *S. cerevisiae* and humans (Asakawa et al., 2014).
93 spNup131 (spNup133a) and spNup132 (spNup133b) have similar molecular

94 structure and both are able to bind to spNup107 (Baï et al., 2004). Despite their similar
95 biochemical features, spNup131 and spNup132 are likely to have different functions
96 because gene disruption strains show different phenotypes. The strain lacking spNup132
97 (*nup132*Δ) displays altered NPC distribution (Baï et al., 2004); its growth is inhibited in
98 the presence of thiabendazole (a microtubule-depolymerizing drug) or hydroxyurea (a
99 DNA replication inhibitor) (Chen et al., 2004; Asakawa et al., 2014); and it exhibits
100 delayed chromosome segregation in meiosis and unusual spore formation (Asakawa et
101 al., 2014; Yang et al., 2015). The strain lacking spNup131 (*nup131*Δ) doesn't display
102 any of these characteristics. In addition, telomere elongation and deficiency in
103 SUMOylation have been reported in *nup132*Δ-specific phenotypes (Liu et al., 2010; Nie
104 and Boddy, 2015). The causes of these functional differences remain unknown.
105 In the present study, we examined the positioning of each Nup within the NPC in *S.*
106 *pombe* using immunoelectron microscopy and high-precision distance measurements
107 using fluorescence microscopy. In addition, genetic interaction analyses were performed
108 to confirm the interaction between certain Nup107-160 components. Our results reveal a
109 unique structure for the *S. pombe* Nup107-160 subcomplex and suggest that a variation
110 in NPC organization developed during evolution in this organism.
111
112 **Results**
113 **spNup131 and spNup132 are differently positioned at the cytoplasmic and**
114 **nucleoplasmic sides of the NPC**
115 The molecular architectures of spNup131 and spNup132 are similar to that found in
116 other species, with an N-terminal β-propeller domain followed by a C-terminal α-helix
117 stack domain (Whittle and Schwartz, 2009) (**Supplementary figure 1a**). However,

118 phylogenetic analysis indicates that spNup131 and spNup132 belong to evolutionarily
119 distant clades, with the spNup131-containing clade branching from a common ancestor
120 of yeast Nup133 homologs much earlier than that of spNup132 (**Supplementary figure**
121 **1b**). This suggests that despite the similarity in their domain architecture, spNup131 and
122 spNup132 may have structural features that are distinct enough to confer different
123 functions.

124 To understand the differences between spNup131 and spNup132, we examined
125 the positioning of those Nups within the NPC by immunoelectronmicroscopy (IEM).
126 The spNup131 or spNup132 gene was replaced with the respective gene N-terminally
127 fused to GFP (GFP-spNup131 or GFP-spNup132). IEM was carried out using a specific
128 antibody against GFP. The results showed that GFP-spNup131 is located at the
129 cytoplasmic side of the NPC, while GFP-spNup132 is located at the nuclear side (**Fig.**
130 **1a**). To confirm the accessibility of the nucleus to immunogold particles using this
131 method, the nuclear centromere protein spMis6 (Saitoh et al., 1997) was co-stained
132 (**Supplementary figure 2a-c**); only the cells positive for spMis6 were evaluated for
133 staining of spNup131(**Supplementary figure 2b, c**). A montage picture of spNup131
134 with quantification shows that spNup131 was exclusively located in the cytoplasmic
135 side of the NPC (left panels of **Fig. 1b**). In contrast, the localization of spNup132 was
136 exclusively in the nuclear side (right panels of **Fig. 1b**), indicating that spNup131 and
137 spNup132 have distinct localizations. To resolve potential artifacts of GFP-tagging at
138 the N-terminus, we repeated these experiments using strains in which spNup131 and
139 spNup132 were C-terminally fused to GFP. We obtained essentially the same results
140 with N- and C-tagged proteins (**Fig. 1c**), suggesting that spNup131 and spNup132 are
141 differentially positioned at the cytoplasmic and nuclear sides, respectively, of the NPC.

142 To confirm the different localization of spNup131 and spNup132 in living cells
143 by fluorescence microscopy (FM), we observed cells simultaneously expressing
144 spNup131 and spNup132 fused with GFP and mCherry, respectively; we also tested
145 cells expressing spNup131 and spNup132 fused with mCherry and GFP, respectively
146 (**Fig. 1d**). To determine their localizations within nuclear pores with high-precision, we
147 applied an open-source program "Chromagnon" (Matsuda et al. 2018; Matsuda A, 2018:
148 this software is available at https://github.com/macronucleus/Chromagnon). After the
149 chromatic correction, the average distance of spNup131 from spNup132 in each nucleus
150 along its radial direction was measured (see Methods for details). As a result, the
151 position of mCherry-spNup132 relative to GFP-spNup131 was -49.3±1.8 nm
152 (mean±SEM), and the position of mCherry-spNup131 relative to GFP-spNup132 was
153 32.7±1.4 nm, both indicating that spNup131 was located at the exterior position (distant
154 from the nuclear center) compared with the location of spNup132 within the NPC (**Fig.**
155 **1e**). These results support the interpretation of the IEM observation that spNup131and
156 spNup132 are separately localized in the NPC: spNup131 is positioned at the
157 cytoplasmic side and spNup132 is positioned at the nucleoplasmic side of the NPC.
158

159 **Different functions of spNup131 and spNup132 at the cytoplasmic and**
160 **nucleoplasmic sides of the NPC**

161 To determine the function of spNup131 and spNup132, we identified its interacting
162 proteins using affinity capture/mass spectrometry (**Supplementary figure 3a,b)**.
163 Several non-Nup proteins that interact with spNup131 and spNup132 were identified
164 (**Supplementary figure 3c**).
165 Among the candidate proteins specifically interacting with spNup131, we

166 selected spFar8 (also known as spCsc3) and examined its functional relationship with
167 spNup131. spFar8 is one of the components of the striatin-interacting phosphatase and
168 kinase (STRIPAK) complex (Goudreault et al., 2009; Frost et al., 2012) that regulates
169 the functions of the spindle pole body (SPB; the yeast microtubule-organizing center)
170 during mitosis (Singh et al., 2011). GFP-fused spFar8 (spFar8-GFP) localized at the
171 nuclear periphery during interphase, as previously reported (Singh et al., 2011) (see
172 "wild type" in **Fig. 2a**). IEM analysis revealed that spFar8-GFP localized at the
173 cytoplasmic side of the nuclear pores (**Fig. 2b**). This NPC localization of spFar8-GFP
174 was greatly decreased in the *nup131*Δ cells (see "*nup131*Δ" in **Fig. 2a**) but not in the
175 *nup132*Δ cells ("*nup132*Δ" in **Fig. 2a)**. Western blotting analysis of the cell strains
176 tested above showed no marked changes in the amount of spFar8 protein (**Fig. 2c**). The
177 mislocalization of spFar8 in the *nup131*Δ cells occurred when spNup132 was
178 ectopically expressed, whereas normal localization was restored when spNup131 was
179 expressed (**Fig. 2d, e**). Localization of another STRIPAK complex protein, spFar11, to
180 the nuclear periphery was also decreased in *nup131*Δ cells (**Supplementary figure 4**).
181 These results suggest that spNup131 plays a role in retaining the STRIPAK complex at
182 the cytoplasmic side of the NPC in interphase cells. The genetic interaction of
183 STRIPAK proteins with spNup131 shown by this experiment is consistent with their
184 localization at the cytoplasmic side of the NPC indicated by IEM.

185 Among the candidate spNup132 interacting proteins identified by affinity
186 capture/mass spectrometry (**Supplementary figure 3c**), we examined the functional
187 relationship of spNup211 with spNup132. spNup211 is an *S. pombe* homolog of human
188 Tpr and *S. cerevisiae* Mlp1 and Mlp2 (Bae et al., 2009); Tpr homologs are known to
189 localize on the nuclear side of the NPC (Strambio-de-Castillia et al., 1999; Krull et al.,

190 2004). IEM analysis of spNup211 showed that spNup211-GFP localized at the nuclear
191 side of the nuclear pores as expected (**Fig. 3a**). To examine its localization in
192 relationship to spNup132, GFP-fused spNup211 (spNup211-GFP) was observed by FM
193 in wild type, *nup131*Δ, and *nup132*Δ cells. In wild type and *nup131*Δ cells,
194 spNup211-GFP was localized at the nuclear periphery (see "wild type" and "*nup131*Δ"
195 in **Fig. 3b**). In contrast, in the *nup132*Δ cells, spNup211-GFP formed several bright foci
196 at the nuclear periphery ("*nup132*Δ" in **Fig. 3b**). We measured the maximum
197 fluorescence intensity of spNup211-GFP in each nucleus in wild type, *nup131*Δ, and
198 *nup132*Δ cells. The value was significantly higher in the *nup132*Δ cells (**Fig. 3c, left**
199 **graph**) whereas spCut11-mCherry, as a control, was uniformly distributed at the nuclear
200 periphery with similar maximum fluorescence intensities in all strains (**Fig. 3c, right**
201 **graph**). This result suggests that the distribution of spNup211 at the NPC is regulated
202 specifically by spNup132 but not spNup131. This fact is consistent with their
203 localizations at the nucleoplasmic side of the NPC, and the lack of interaction between
204 spNup211 and spNup131 is also consistent with their different localizations within the
205 NPC.
206
207 **Immunoelectron microscopy of spNup107-160 subcomplex Nups**
208 Because the Nup133 homologs are integrated components of the Nup107-160
209 subcomplex, we next examined the positioning of the other Nup107-160 subcomplex
210 components in *S. pombe*: spNup107 (scNup84/hsNup107), spNup120
211 (scNup120/hsNup160), spNup85 (scNup85/hsNup85), spNup96 (also known as
212 spNup189C; scNup145C/hsNup96), spNup37 (hsNup37), spEly5 (hsELYS), and
213 spSeh1 (scSeh1/hsSeh1) in cells expressing each of these Nups fused to GFP. A

214 spNup98-spNup96 fusion protein is expressed as the *nup189*$^{+}$ gene product, and
215 spNup96 is generated by cleavage with the autopeptidase activity in the C-terminus of
216 spNup98 (Asakawa et al., 2015).

217 IEM results showed that of the 7 Nups, spNup120, spNup85, spNup96,
218 spNup37, spEly5, and spSeh1 were predominantly located on the cytoplasmic side of
219 the NPC, whereas spNup107 was located on the nuclear side of the NPC (**Fig. 4a**). The
220 localization of spNup107 on the nuclear side was also confirmed using an N-terminus
221 fusion protein (**Fig. 4a**). Simultaneous detection of spMis6-GFP further confirmed the
222 localization of spNup120, spNup85, spNup96, spNup37, spEly5 and spSeh1 on the
223 cytoplasmic side of the NPC (**Fig. 4a**). This result suggests that the Nup107-160
224 subcomplex is split into two pieces in *S. pombe* and that these two pieces are differentially
225 located on the cytoplasmic and nuclear sides of the NPC. This result contrasts with the
226 structure of the Nup107-160 complex reported in *S. cerevisiae* and humans, in which all
227 of the components are connected to form the Y-shape structure. Thus, this result
228 suggests an unexpected separation of the Nup107-160 subcomplex at the junction of
229 spNup96 and spNup107 in *S. pombe*.

230 To confirm the different localizations of the Nup107-160 subcomplex
231 components by FM, we examined the localization of these components in living cells.
232 We chose spNup85 and spNup107 as representatives of cytoplasmic and nucleoplasmic
233 components identified by IEM. We first determined the position of spNup85-GFP
234 within NPCs by comparing it with that of mCherry-spNup131 and mCherry-spNup132
235 (**Fig. 4b**). The position of mCherry-spNup131 relative to spNup85-GFP was 11.4±1.9
236 nm (mean±SEM) and the position of mCherry-spNup132 relative to spNup85-GFP was
237 -26.2±1.0 nm (**Fig. 4b**; the relative position of Nup85 to Nup131 and Nup132 is

indicated in the right panel). This result supports cytoplasmic positioning of spNup85 as indicated by IEM. Second, we determined the position of spNup107-GFP within NPCs using a similar method. The position of mCherry-spNup131 relative to spNup107-GFP was 34.0±2.1 nm and the position of mCherry-spNup132 relative to spNup107-GFP was -4.4±1.0 nm (**Fig. 4c**; the relative position of Nup107 to Nup131 and Nup132 is indicated in the right panel). This result supports nuclear positioning of spNup107 as indicated by IEM.

Taken together, these results demonstrate that the Nup107-160 subcomplex components are differentially localized at the cytoplasmic and nucleoplasmic sides within the NPC in *S. pombe* (**Fig. 4d**). Based on the localization analysis in this study and quantification of each Nup reported previously (Asakawa et al., 2014), we estimated the molecular weight of the cytoplasmic outer ring and nucleoplasmic outer ring as 7.4 MDa and 7.0 MDa, respectively: the cytoplasmic outer ring is estimated as 8-fold of a single unit (two each of spNup120, spNup85, spNup96, spEly5, and spNup37 and one each of spSeh1 and spNup131), and the nucleoplasmic outer ring is estimated as 8-fold of a single unit (six spNup132 and one spNup107). In this estimation, a single unit of both the cytoplasmic and nucleoplasmic outer rings consist of 7 α-solenoids and 6 β-propellers as elements, suggesting that the ring structures are similar to each other. The values are a bit larger than the molecular weight (4.65 MDa) of one outer ring in *S. cerevisiae*, which consists of 8-fold of a single unit containing 5 α-solenoids and 4 β-propellers as elements (Kim et al., 2018).

Enforced cytoplasmic localization of Nup107 by fusing to Nup96 results in reduction of Nup132 from the nuclear side, leading to defects in meiosis

262 To address the significance of the separated localization of the *S. pombe* Nup107-160
263 subcomplex components, we generated an *S. pombe* strain with spNup96 artificially
264 fused to spNup107 in a *nup107*Δ background (spNup96-spNup107-GFP). The strain
265 was viable, and Western blot analysis confirmed expression of the fusion protein with
266 the predicted molecular weight (**Fig. 5a**). By IEM, the majority of the
267 spNup96-spNup107-GFP fusion protein molecules were localized at the cytoplasmic
268 side of the NPC (**Fig. 5b**), showing a change in the location of spNup107 from the
269 nuclear side to the cytoplasmic side. Under this condition, spNup132 was recruited to
270 both the nuclear and cytoplasmic sides of the NPC (**Fig. 5c**), suggesting that a
271 significant fraction of the spNup132 molecules was recruited by spNup107. We
272 assumed that the cytoplasmic recruitment of spNup132 molecules would result in a
273 reduction of spNup132 at the nuclear side. As previously reported, the *nup132*Δ cells
274 exhibit growth sensitivity to the microtubule-destabilizing drug thiabendazole (TBZ),
275 and they have delayed meiotic division and abnormal spore formation (Chen et al, 2004;
276 Asakawa et al, 2014; Yang et al, 2015). Thus, we examined whether the
277 spNup96-spNup107-GFP strain showed those deficiencies. We found that this strain
278 exhibited growth sensitivity to TBZ (**Fig. 5d)**, delayed meiotic division (**Fig. 5e, f**), and
279 abnormal spore formation (**Fig. 5g**), similarly to the defects found in *nup132*Δ cells.
280 These results suggest that the split structure and asymmetrical localization of the
281 Nup107-160 subcomplex are necessary for retaining Nup132 at the nuclear side of the
282 NPC, which in turn is necessary for the normal progression of mitosis and meiosis in *S.*
283 *pombe*.
284
285 **The N-terminal β-propeller region is required for differential localization of**

286 **Nup133 homologs**

287 Finally, we determined which domains of spNup131 and spNup132 were responsible for
288 their different localizations. In this experiment, we expressed full length spNup131 or
289 spNup132, fragments of spNup131 or spNup132, or chimeric proteins of spNup131 and
290 spNup132 (**Fig. 6a**). To exclude the possibility that endogenous spNup131 or spNup132
291 predominantly occupy preferred sites for spNup131 and spNup132 fragments or
292 chimeric proteins, a *nup131*Δ *nup132*Δ double-deletion strain (lacking genes for both
293 spNup131 and spNup132) was used. Protein expression was confirmed by Western blot
294 analysis (**Supplementary figure 5**). FM observation showed that GFP fused full-length
295 spNup131 (spNup131FL) and spNup132 (spNup132FL) were localized at the nuclear
296 periphery (**Fig. 6b**). The N-terminal domains of both Nup131 and Nup132 (spNup131N
297 and spNup132N) were not localized at the nuclear periphery, while the C-terminal
298 domain of both proteins (spNup131C and spNup132C) were localized at the nuclear
299 periphery, consistent with a previous report (Berke et al., 2004). Interestingly, IEM
300 analysis showed that spNup131C localized to the nuclear side of the NPC (**Fig. 6c**) in
301 contrast with the localization of full length spNup131 on the cytoplasmic side (compare
302 the upper two panels in **Fig. 6c**; also see **Fig. 1b**). These results suggest that the
303 C-terminal domains of both spNup131 and spNup132 have the ability to localize on the
304 nuclear side of the NPC, probably through binding to Nup107, and also suggest that the
305 N-terminal domains of spNup131 and spNup132 are involved in determining their
306 differential localizations. To test this idea, we examined the localization of the chimeric
307 proteins spNup131N+spNup132C and spNup132N+spNup131C: If the C-terminal
308 domains were independent and functioning correctly, both chimeric proteins should be
309 localized to the nuclear side of the NPC via interaction with Nup107, and if the

310 N-terminal domains were independent and functioning correctly, the
311 spNup131N+spNup132C protein should then be localized to the cytoplasmic side via
312 Nup131N and the spNup132N+spNup131C protein should be retained on the nuclear
313 side via Nup132N. The results showed that the spNup131N+spNup132C chimeric
314 protein mostly diffused to the cytoplasm with some enrichment in the nuclear periphery
315 compared with spNup132FL (**Fig. 6b**) and that the other chimeric protein,
316 spNup132N+spNup131C, also diffused to the cytoplasm but with no enrichment in the
317 nuclear periphery compared with spNup131FL (**Fig. 6b**). The relatively strong
318 cytoplasmic staining of the chimeric proteins suggests that the N-terminal domains may
319 function to prevent "abnormal" localization of spNup131 and spNup132. Overall, this
320 result indicates that both N-terminal and C-terminal domains are required for the proper
321 differential localization of spNup131 and spNup132.
322
323 **Immunoelectron microscopy of the other nucleoporins**
324 Because the Nup107-160 subcomplex seems to have a unique organization in *S. pombe,*
325 we wished to understand the overall structure of the NPC. For this purpose, we
326 performed IEM of other Nups to reveal their positionings within the NPC. GFP-fused
327 Nups were used and IEM was carried out using a specific antibody against GFP, unless
328 specified otherwise (**Fig. 7**). We first examined inner ring Nups known as the Nup93
329 subcomplex in vertebrates. spNup97 and spNpp106, redundant *S. pombe* homologs of
330 scNic96/hsNup93, were both similarly positioned near the center of the NPC (**Fig. 7a**);
331 the redundancy of scNic96/hsNup93 homologs is unique to the *Schizosaccharomyces*
332 genus. spNup184 (scNup188/hsNup188) and spNup186 (scNup192/hsNup205) were
333 also positioned near the center (**Fig. 7a**). spNup40 (scNup53/scNup59/hsNup35) and

334 spNup155 (scNup157/scNup170/hsNup155) were also located near the center of the
335 NPC, but they showed a slightly broader range of localization (**Fig. 7a**).
336 The channel Nups spNup44 (scNup57/hsNup54) and spNup45
337 (scNup49/hsNup58) were positioned at the center of the pore (**Fig. 7b**). spNup98
338 (scNup145n/hsNup98) was detected on the cytoplasmic side of the nuclear pore when
339 using an anti-GFP antibody (see "spNup98-GFP" in **Fig. 7b**); however, an anti-Nup98
340 antibody (clone 13C2; Iwamoto et al., 2013), which specifically recognizes endogenous
341 spNup98, detected its positioning near the center of the pores (see "spNup98" in **Fig.**
342 **7b**). This staining pattern is likely due to the interaction of spNup98 with other Nups. In
343 *H. sapiens* and *S. cerevisiae*, the C-terminal region of the Nup98 homologs
344 (hsNup98/scNup145n/scNup100/scNup116) interacts with Nup96 homologs
345 (hsNup96/scNup145c) (Hodel et al., 2002; Griffis et al., 2003; Ratner et al., 2007;
346 Stuwe et al., 2012), and the C-terminal Nup98-APD (autoproteolytic and NPC-targeting
347 domain) binds to Nup88 homologs (hsNup88/scNup82) and to Nup96 in a mutually
348 exclusive manner (Stuwe et al., 2012). Thus, the C-terminal region of spNup98 might be
349 tethered by spNup96 and spNup82, both of which are positioned at the cytoplasmic side
350 of the NPC, while the N-terminal region is extended to the center of the pore. The *S.*
351 *pombe* homolog of the conserved Nup Nsp1 (scNsp1/hsNup62) was localized
352 frequently in the cytoplasmic side and infrequently in the nuclear side of the NPC (**Fig.**
353 **7b**).
354 spNup82 (scNup82/hsNup88) and spNup146 (scNup159/hsNup214) were
355 detected at the cytoplasmic side (**Fig. 7c**) as expected from their homologous
356 counterparts. spAmo1(scNup42/hsNlp1) was also detected at the cytoplasmic side (**Fig.**
357 **7c**). The transmembrane Nups, spCut11 (scNdc1/hsNdc1), spPom152 (scPom152), and

358 spPom34 (scPom34) were localized at the center of the pore and slightly biased toward
359 the cytoplasm (**Fig. 7d**). The conserved Nups, spNup60 (scNup60), spNup61
360 (scNup2/hsNup50), and spNup124 (scNup1/hsNup153) (**Fig. 7e)** as well as
361 spNup211(scMlp1/scMlp2/hsTpr) (**Fig. 3a**) were detected at the nuclear side as
362 expected from their homologous counterparts. We added a recently identified Nup
363 spAlm1 (Salas-Pino et al., 2017) to the group of nuclear Nups, according to its
364 nucleoplasmic localization **(Fig. 7e)**.

365 We summarized the positionings of the *S. pombe* Nups within the NPC in **Fig.**
366 **8**. Transmembrane Nups (spCut11, spPom152, and spPom34); inner ring Nups
367 (spNup97, spNpp106, spNup184, spNup186, spNup40, and spNup155); cytoplasmic
368 ring Nups (spNup82, spNup146, spAmo1, spNsp1); central channel Nups (spNsp1,
369 spNup98, spNup44, and spNup45); and nuclear basket Nups (spNup124, spNup60,
370 spNup61, spNup211, and spAlm1) are positioned similarly to the positions of their
371 orthologs in *S. cerevisiae* and human (Rout et al., 2000; Maimon et al., 2012; Bui et al.,
372 2013: von Appen et al., 2015; Kim et al., 2018). Thus, these NPC substructures, which
373 include a central channel structure that is required for nucleocytoplasmic transport,
374 seem to be common to other eukaryotes. In contrast, the Nup107-160 subcomplex
375 (spNup131, spNup120, spNup85, spNup96, spNup37, spEly5 and spSeh1, spNup107
376 and spNup132) in *S. pombe* has a highly unusual asymmetrical organization: spNup131,
377 spNup120, spNup85, spNup96, spNup37, spEly5 and spSeh1 are located in the
378 cytoplasmic side of the NPC whereas spNup107-and spNup132 are located in the
379 nuclear side of the NPC. This asymmetrical organization of the Nup107-160
380 subcomplex may be required for building and maintaining the structural organization of
381 the central channel and other NPC elements common to other eukaryotes, and

382 consequently, the Nup107-160 subcomplex would be required for normal cell cycle
383 progression in *S. pombe.*
384
385 **Discussion**
386 IEM of *S. pombe* Nups suggest that the *S. pombe*-specific Nup107-160 subcomplex
387 structure is uniquely split into two pieces that localize differentially to the cytoplasmic
388 and nuclear sides of the NPC while preserving the conserved modular structures of the
389 Nup107-160 subcomplexes of other eukaryotes. High-precision distance measurements
390 using FM also support this result (**Fig. 1d,e, and 4b**). The asymmetrical organization of
391 the *S. pombe* Nup107-160 subcomplex contrasts with the localization of the
392 Nup107-160 subcomplexes in *H. sapiens*, *S. cerevisiae* and *Trypanosoma brucei*, in
393 which Nup107-160 complexes are found on both the cytoplasmic and nuclear sides of
394 the NPC (Rout et al., 2000; D'Angelo et al., 2006; von Appen et al., 2015; Obado et al.,
395 2016a; Kim et al., 2018). Our results suggest that the *S. pombe* NPC has a novel
396 organization that has evolved in the *Schizosaccharomyces* genus, which commonly
397 bears the Nup132 and Nup131 clades (**Supplementary figure 1b**).
398 In *H. sapiens* and *S. cerevisiae,* the Nups in the Nup107-160 subcomplex
399 assemble to form Y-shaped structures (Lutzmann et al., 2002; Kampmann and Blobel,
400 2009; Kelley et al., 2015; Stuwe et al., 2015; von Appen et al., 2015). A total of 32
401 Y-complexes form two concentric reticulated rings at both the nuclear and cytoplasmic
402 sides of the human NPC (Bui et al., 2013; von Appen et al., 2015). This organization
403 may be supported by the iso-stoichiometry of each Nup in the Nup107-160 subcomplex:
404 the amounts of each Nup in the Nup107-160 subcomplex in human cells are nearly
405 equal (Ori et al., 2013). In contrast, in *S. pombe*, the amounts of each Nup in the

406 Nup107-160 subcomplex are not equal but highly divergent, ranging from 1 copy to 5-6
407 copies/unit (Asakawa et al., 2014). In addition, the Sec13 homolog in *S. pombe* does not
408 localize in the NPC, and Nup43 is not conserved in the genome (Asakawa et al., 2014).
409 The different stoichiometry and composition of the *S. pombe* Nup107-160 subcomplex
410 components are likely due to the unique fission yeast–specific separated structure of the
411 Nup107-160 subcomplex revealed in this study.

412 The role of the separate locations of the Nup107-160 subcomplex remains
413 unknown. In mammalian cells undergoing 'open mitosis,' the Nup107-160 subcomplex
414 is required for NPC assembly at an early stage of telophase and is therefore thought to
415 provide a structural element important for reconstructing the NPC at the end of mitosis
416 (Walther et al., 2003; Harel et al., 2003; Boehmer et al., 2003). Thus, the Nup107-160
417 subcomplex has essential scaffold functions. In contrast, during vegetative cell growth
418 in fungi mitosis is 'closed'. Consequently, the nuclear envelope is not broken down
419 during mitosis and the NPCs do not need to be reconstructed. Notably, Nup133
420 homologues are dispensable for vegetative growth in fungi, including *S. pombe* and *S.*
421 *cerevisiae* (Doye et al., 1994; Baï et al., 2004; Asakawa et al., 2014). This suggests a
422 different role for Nup133 homologs among eukaryotes depending on the type of mitosis.
423 While the role of Nup133 homologs in vegetative cell growth in fungi is unknown, it is
424 clear that spNup132 but not spNup131 is required for the progression of meiosis in *S.*
425 *pombe*, especially with regard to proper segregation of meiotic chromosomes (Asakawa
426 et al., 2014; Yang et al., 2015). Such functional differences between spNup131 and
427 spNup132 are reflected by the different locations of these two components within the
428 NPC (**Fig. 1**). A decrease in spNup132 on the nuclear side and its relocation to the
429 cytoplasmic side causes defects in meiosis similar to those found in *nup132Δ* cells as

430 shown in Figure 5, further supporting our conclusion.

431 spNup132 is required for normal kinetochore formation during meiosis in *S.*
432 *pombe*. Deletion of the *nup132* gene but not the *nup131* gene causes untimely
433 kinetochore assembly during the first meiotic chromosome segregation (Yang et al.,
434 2015) and increases the sensitivity to the microtubule-destabilizing drug thiabendazole,
435 likely due to defects in the kinetochore structure in mitosis (Asakawa et al., 2014).
436 Similarly, in mammalian cells, kinetochore-related functions have been reported for the
437 Nup107-160 subcomplex. A fraction of the Nup107-160 subcomplex is found at the
438 kinetochores and spindle poles during mitosis (Harel et al., 2003; Loïodice et al., 2004;
439 Belgareh et al., 2001; Orjalo et al., 2006), and depletion of the Nup107-160 subcomplex
440 from kinetochores results in altered kinetochore protein recruitment (Zuccolo et al.,
441 2007; Platani et al., 2009; Mishra et al., 2010). While the molecular mechanism of
442 underlying spNup132-mediated regulation of kinetochore proteins remains unknown,
443 considering the similarity in kinetochore-related functions, spNup132, but not
444 spNup131, is likely to be a functional homolog of mammalian Nup133.

445 IEM analysis in this study revealed that spNup131 is localized only on the
446 cytoplasmic side of the NPC, and a genetic analysis showed interaction between
447 spNup131 and spFar8. spFar8, which was proven to be located at the cytoplasmic side
448 of the NPC in this study, is an *S. pombe* ortholog of the STRIPAK complex component
449 Striatin (Frost et al., 2012). In *S. pombe*, the STRIPAK complex regulates the septation
450 initiation network through the conserved protein kinase Mob1 (Moreno et al., 2001;
451 Goudreault et al., 2009) and is required for asymmetric division of mother and daughter
452 SPBs during mitosis (Singh et al., 2011). The spNup131-dependent NPC localization of
453 spFar8 revealed by this study implies that the NPC regulates STRIPAK localization in

454 interphase cells. Human STRIPAK complexes have been proposed to play roles at the
455 interface between the Golgi and the outer nuclear envelope (Frost et al., 2012).
456 Considering the physical and genetic interaction with spNup131, STRIPAK is likely to
457 interact with the NPC on the cytoplasmic side of the NE. Although the role of the
458 STRIPAK complex in interphase cells in *S. pombe* is not fully understood, the
459 interaction between spNup131 and spFar8 may provide an important example linking
460 the NPC to cytoplasmic structures.

461 This study demonstrates that the *S. pombe* Nup107-160 subcomplex has a
462 novel separated structure and exhibits a localization pattern not reported in other
463 organisms. Recent studies suggest that NPC structures are not necessarily the same
464 among eukaryotes (Iwamoto et al., 2017; Mosalaganti et al. 2018; Kim et al., 2018). For
465 example, the binucleated ciliate *Tetrahymena thermophila,* a single-cell organism, has
466 two functionally distinct nuclei, the macronucleus (MAC) and micronucleus (MIC), in a
467 single cell: The MAC and MIC differ in size, transcriptional activity, and
468 nucleocytoplasmic transport specificity (Karrer, 2012). Interestingly, in *T. thermophila,*
469 the MAC and the MIC NPCs are composed of differ amounts of the Nup107-160
470 subcomplex components (Iwamoto et al., 2017). The amount of the subcomplex in the
471 MIC is about three times more than that in the MAC, suggesting that the Nup107-160
472 subcomplex forms different structures in the MAC from the MIC. In the green algae
473 *Chlamydomonas reinhardtii*, a single cell organism, the NPCs have 24 Y-complexes
474 asymmetrically distributed within a single NPC: 16 Y-complexes at the nuclear side and
475 eight Y-complexes at the cytoplasmic side (Mosalaganti et al. 2018). The asymmetrical
476 distribution of the Y-complexes in *C. reinhardtii* may suggest a specific function of the
477 Y-complex in either cytoplasmic or nuclear side of the NPC although it is currently

unclear. In some multicellular organisms, the expression level of Nups varies between cell types and during development (Ori et al., 2013; Cho et al., 2009; Olsson et al., 2004; D'Angelo et al., 2009; D'Angelo et al., 2012). It is also known that some mutations in Nups result in developmental defects in metazoans (Raices and D'Angelo, 2012). These findings suggest that the NPC composition in cell types and during development is biologically significant. Altered compositions might alter the NPC structure, at least in part; thus, unidentified NPC subcomplex structures may play roles in specific biological events such as differentiation and development. Thus, we speculate that novel NPC structures may be important to elucidate the biological functions of the NPC.

Methods

S. pombe cell cultivation

Strains used in this study are listed in Supplementary Table 1. YES or EMM2 culture medium was used for routine cultures (Moreno et al., 1991). ME medium was used to induce meiosis and spore formation. When necessary, TBZ (T5535-50G, Sigma-Aldrich Inc, Tokyo, Japan) was added to the YES medium to a final concentration of 10 μg/mL.

Immunoelectron microscopy

For immunoelectron microscopy, 1.5×10^8 cells expressing GFP-Nup131 were fixed in 1 mL of a mixture of 4% formaldehyde (18814-10, Polysciences, Inc, Warrington, PA, USA) and 0.01% glutaraldehyde (1909-10, Polysciences, Inc.) dissolved in 0.1 M phosphate buffer (PB) (pH 7.4) for 20 min at room temperature, treated with 0.5 mg/mL Zymolyase 100T (7665-55, Nacalai Tesque, Inc., Kyoto, Japan) in PB for 20-30 min at

30°C, and then permeabilized with 0.2% saponin (30502-42, Nacalai Tesque, Inc.) and 1% bovine serum albumin (BSA) in PB for 15 min. The GFP epitope tag was labeled with a primary antibody (600-401-215, rabbit polyclonal anti-GFP antibody, Rockland Immunochemicals, Limerick, PA, USA) diluted 1:400 in PB containing 1% BSA and 0.01% saponin, and a secondary antibody (7304, goat anti-rabbit Alexa 594 FluoroNanogold Fab' fragment; Nanoprobes Inc., Yaphank, NY, USA) diluted 1:400. The same immunostaining conditions were used for the cells expressing each of the other GFP-fused Nups except for the dilution ratios of primary and secondary antibodies; the conditions used for each experiment are listed in supplementary Table 2. For analysis of the spNup98 N-terminal region, we used a mouse monoclonal anti-Nup98 antibody (13C2) (Iwamoto et al., 2013; Asakawa et al., 2015; available from BioAcademia Inc, Japan, Cat. #70-345) diluted 1:100 and anti-mouse Alexa594 FluoroNanogold Fab' fragment (7302, Nanoprobes) diluted 1:400. Cells then were fixed again with 1% glutaraldehyde in PB for 1 h at room temperature and treated with 100 mM lysine HCl in PB twice for 10 min each. The cells were stored at 4°C until use. Before use, the cells were incubated with 50 mM HEPES (pH 5.8) three times for 3 min each and with distilled water (DW) once, incubated with Silver enhancement reagent (a mixture of equal volumes of the following A, B, and C solutions: A, 0.2% silver acetate solution; B, 2.8% trisodium citrate-$2H_2O$, 3% citric acid-H_2O, and 0.5% hydroquinone; C, 300 mM HEPES, pH 8.2) at 25°C for 2-5 min. Cells were embedded in 2% low melting agarose dissolved in DW. Cells were post-fixed with 2% OsO_4 in DW for 15 min and stained with 1% uranyl acetate in DW at room temperature. Cells were dehydrated using stepwise incubations in ethanol and acetone and finally embedded in epoxy resin Epon812. Solidified blocks containing cells were sectioned, and the

526 ultra-thin sections were stained with uranyl acetate and lead citrate, the usual
527 pretreatment for EM observations. Images were obtained using a JEM1400 transmission
528 electron microscope (JEOL, Tokyo, Japan) at 120kV.
529 Nuclear pores containing more than two immunogold particles were chosen for
530 localization analysis as described previously (Rout et al., 2000). To confirm the
531 accessibility of the nucleus to immunogold particles, the nuclear centromere protein
532 spMis6-GFP was co-expressed with GFP-fused Nups in cells and stained with anti-GFP
533 antibody for IEM. For quantification of the Nup signals, we chose only cell specimens
534 with a positive spMis6-GFP signal. For quantitative representations, montage pictures
535 were produced by stacking 20 NPC images with 5% opacity on Adobe Photoshop CS
536 software.
537
538 ***cDNA clones***
539 *nup107*$^{+}$ and *nup37*$^{+}$ cDNAs were provided by National BioResource Project Japan
540 (http://yeast.lab.nig.ac.jp/yeast/top.xhtml). cDNA fragments of other Nups were
541 amplified from a cDNA library pTN-RC5 or pTN-FC9 (National BioResource Project
542 Japan) using PCR.
543
544 ***Strain construction***
545 To visualize nuclear pore localization of the different domains of Nup131 and Nup132,
546 *lys1*$^{+}$-integrating plasmids carrying GFPs65t-fused with respective Nup domains were
547 introduced into cells with a *nup131*Δ*nup132*Δ double-deletion mutant background. To
548 construct the spNup96-spNup107 fusion Nup, a cDNA fragment encoding spNup107 or
549 spNup107-GFP followed by a drug resistance marker gene was integrated after the

550 chromosomal spNup96 coding region. After a diploid strain was obtained by crossing
551 the spNup96-spNup107 fusion containing strain with the wild type strain, the *nup107*$^{+}$
552 gene on the original chromosomal locus was deleted. To introduce the chromosomal
553 fluorescent tag and gene disruption, a two-step PCR method was applied (Bähler et al.,
554 1998). Nup-GFP fusion constructs were described previously (Asakawa et al., 2014).
555 The spMis6-GFP fusion was constructed as described previously (Chikashige et al.,
556 2004) or using the two-step PCR method. mCherry-spAtb2 was visualized as described
557 previously (Yang et al., 2015).
558
559 ***Plasmid construction***
560 To express the full-length or domains of the spNup131 and spNup132 proteins, cDNA
561 fragments were amplified by PCR. For overexpression, the PCR products were
562 sub-cloned into the plasmid that carries the *nmt1* promoter and terminator. For
563 physiological expression, the PCR products were sub-cloned into the *Bgl*II site of the
564 plasmid (pY53) that carries the *nup132* promoter (-1000bp)-driven GFPs65t and the
565 *nmt1* terminator. Each sub-cloning was done by using the In-Fusion PCR cloning kit
566 (Clontech Laboratories, Mountain View, CA, USA). Plasmids were integrated at the
567 *lys1* gene locus. Correct integrations were confirmed by PCR.
568
569 ***Fluorescence microscopy***
570 Images were obtained using a DeltaVision microscope system (GE Healthcare, Tokyo,
571 Japan) equipped with a CoolSNAP HQ^{2} CCD camera (Photometrics, Tucson, AZ, USA)
572 through an oil-immersion objective lens (PlanApoN60×OSC; NA, 1.4) (Olympus,
573 Tokyo, Japan) as described previously (Asakawa et al., 2014). Z-stack images were

574 obtained and processed by deconvolution and denoising algorithm (Boulanger et al.
575 2009) when necessary. For time lapse microscopy, cells were observed every 5 minutes
576 as described previously (Yang et al., 2015). The projection images of z-stacks were
577 made by softWoRx software equipped in the microscope system.
578
579 ***Precise distance measurements with fluorescence microscopy***
580 Cells to be analyzed were cultured in 150 µl of the EMM2 5S medium on an 8-well
581 chambered coverglass, Lab-Tek II (Thermo Fisher Scientific Japan, Yokohama, Japan);
582 cells used for references for chromatic correction were also cultured in a chamber of the
583 same coverglass. Simultaneously acquired multicolor images were obtained with OMX
584 SR (GE Healthcare) equipped with three sCMOS cameras. The three-dimensional (3D)
585 images were deconvolved by constrained iterative deconvolution using the Priism suite
586 (http://msg.ucsf.edu/IVE/) with a Wiener filter enhancement of 0.9 and 15 iterations. To
587 correct for chromatic shifts of multicolor FM images, green-to-red photoconversion of
588 GFP was used as the reference as previously reported (Sawin and Nurse 1997; Matsuda
589 et al., 2010): Nup96-GFP was used in this study. For photoconversion, cells were
590 illuminated with 405 nm light at about 393 W/cm^2 for 4 seconds, then both green and
591 red-converted GFP species were excited with 488 nm to obtain images of the same
592 object in the green and red channels. Chromatic shifts were measured using such images,
593 and the correction parameters were determined using the Chromagnon software
594 (https://github.com/macronucleus/Chromagnon), by which a chromatic shift can be
595 corrected with an accuracy of ~10 nm in 2D XY plane and ~15 nm in 3D XYZ space
596 using test samples (Matsuda et al., 2018). The correction parameters were applied to all
597 images obtained from the same chambered coverglass as described in Matsuda et al.,

598 2018.

599 Next, individual nuclei in the images were identified and segmented by our
600 software using functions from the “ndimage” module of the Scipy package
601 (http://www.scipy.org). The centers of the nuclei were identified by least-square fitting
602 with 3D ellipses using the 3D coordinates of the nucleoporin fluorescence above
603 threshold. The images of the NE at the midsection were linearized with polar
604 transformation. These images were then averaged across all angles to produce 1D
605 intensity profiles along the radial direction of the nuclei. The intensity profiles were
606 fitted to Gaussian profiles to determine a distance between the peaks of green and red
607 for each of the individual nuclei. The mean distance was determined from more than 70
608 nuclei. Because not all nuclei were round, we rejected nuclei of elliptical or irregular
609 shapes before the final calculation.

610

611 ***Western blot analysis***

612 For western blot analysis, whole cell extracts were prepared from approximately 5×10^6
613 cells by trichloroacetic acid (TCA) precipitation as described previously (Asakawa et al.,
614 2014). To detect GFP-fused proteins, a rabbit polyclonal anti-GFP antibody
615 (600-401-215, Rockland Immunochemicals Inc.) was used. To detect spNup98, a mouse
616 monoclonal anti-Nup98 antibody (13C2) was used (Iwamoto et al., 2013).
617 HRP-conjugated goat anti-rabbit or anti-mouse IgG (NA9340-1ml or NA9310-1ml, GE
618 Healthcare) was used as a secondary antibody. Protein bands were detected by
619 chemiluminescence using ChemiDoc MP imaging system (Bio-Rad).

620

621 ***Preparation of whole cell extracts for affinity-capture experiments***

622 Growing cells (about 5×10^9) were collected and washed with 10 mM HEPES buffer
623 (pH 7.5) containing 1 mM phenylmethylsulfonyl fluoride (PMSF). The washed cells
624 were divided into aliquots of 3×10^8 cells in 10 mM HEPES buffer (pH 7.5) containing
625 1 mM PMSF. Cells were again collected by centrifugation, and the cell pellet was kept
626 frozen by liquid nitrogen until use. To make a cell extract, the cell pellet was thawed
627 and suspended in 100 μL of lysis buffer (50 mM HEPES (pH 7.5), 150 mM NaCl, 1%
628 Triton X-100, 1 mM EDTA, 2 mM PMSF) with a protease inhibitor cocktail (165-20281,
629 Wako, Tokyo, Japan) and mashed by glass beads using Multi-beads shocker (Yasui
630 Kikai Corporation, Osaka, Japan). We chose this extraction condition based on a
631 previous study identifying the components of plant NPCs (Tamura et al., 2010).
632 Because the presence of 1% Triton X-100 gave better results for extracting plant NPC
633 components, we decided to use 1% Triton X-100 as a detergent, and we examined three
634 different salt conditions (50 mM, 150 mM or 500 mM NaCl) in the presence of the
635 detergent. As a result, 150 mM NaCl gave better results with low background. At least
636 for extracting spNup131 and spNup132, this condition was better than that optimized
637 for extracting NPCs in other organisms such as budding yeast (1.5 M ammonium
638 acetate, 1% Triton X-100) (Hakhverdyan et al., 2015) and trypanosoma (20 mM HEPES
639 (pH7.4), 250 mM NaCitrate, 0.5% Triton X-100, 0.5% deoxy Big CHAP) (Obado et al.,
640 2016b). After further addition of 400 μL of lysis buffer, the mashed cell pellet was
641 transferred to new microtubes. The supernatant was collected after centrifugation at
642 15000 rpm for 15 min at 4°C and used as the whole-cell extract.
643
644 ***Affinity-capture and LC/MS/MS analysis***
645 The whole-cell extract was incubated with a rabbit anti-GFP antibody (600-401-215,

646 Rockland Immunochemicals). Antibody-conjugated proteins were collected by
647 incubating with Protein A Sepharose beads (17528001, GE Healthcare). Beads were
648 then washed 4-5 times with the lysis buffer described above. After elution in
649 SDS-PAGE sample buffer, protein samples were loaded onto a 12% SDS-PAGE gel for
650 liquid chromatography coupled to tandem MS (LC/MS/MS). Data analysis for
651 LC/MS/MS was performed as described previously (Nozawa et al., 2013) using the
652 Pombase protein dataset released on November 12th, 2015. To identify proteins
653 interacting with spNup131 and spNup132, protein samples were prepared from two
654 independent experiments and each preparation was analyzed by LC/MS/MS. Proteins
655 detected as more than one unique spectrum were identified as interacting proteins with
656 spNup131 and spNup132. Alternatively, when proteins detected as only one unique
657 spectrum in the first experiment were repeatedly detected in the second experiment,
658 they were also identified as interacting proteins.
659

660 **Acknowledgements**

661 We thank the National BioResource Project Japan for the Nup cDNA clones. We also
662 thank Drs. Thomas U. Schwartz, Valérie Doye, and David B Alexander for critical
663 reading of this paper. This work was supported by the Uehara Memorial Foundation to
664 TH, by grant from Ministry of Science and Technology (107-2321-B-400-014-MY3) to
665 HJY and by the following JSPS KAKENHI grants: JP26440098 to HA; JP15K07066 to
666 MI; JP17K07249 to YC; JP15K06942 and JP15H01462 to KN; JP16H04739 and JP
667 25116004 to COb; JP26251037, JP16H01309, and JP18H05533 to YH; JP25116006,
668 JP26291007, JP17K19505, JP18H05528 to TH.
669

670 **Competing financial interests**

671 The authors declare no competing financial interests.

672

673

674

675 **References**

676 Alber F, Dokudovskaya S, Veenhoff LM, Zhang W, Kipper J, Devos D, Suprapto A,
677 Schmidt OK, Williams R, Chait BT, Sali A. Rout MP. 2007. The molecular
678 architecture of the nuclear pore complex. Nature 450: 695-701.
679 doi:10.1038/nature06405

680 Amlacher S, Sarges P, Flemming D, van Noort V, Kunze R, Devos DP, Arumugam M,
681 Bork P, Hurt E. 2011. Insight into structure and assembly of the nuclear pore
682 complex by utilizing the genome of a eukaryotic thermophile. Cell 146: 277-286.
683 doi:10.1016/j.cell.2011.06.039.

684 Asakawa H, Yang HJ, Yamamoto TG, Ohtsuki C, Chikashige Y, Sakata-Sogawa K,
685 Tokunaga M, Iwamoto M, Hiraoka Y, Haraguchi T. 2014. Characterization of
686 nuclear pore complex components in fission yeast *Schizosaccharomyces pombe*.
687 Nucleus. 5: 149-162. doi:10.4161/nucl.28487

688 Asakawa H, Mori C, Ohtsuki C, Iwamoto M, Hiraoka Y, Haraguchi T. 2015.
689 Uncleavable Nup98-Nup96 is functional in the fission yeast *Schizosaccharomyces*
690 *pombe*. FEBS Open Bio. 5: 508-514. doi:10.1016/j.fob.2015.06.004.

691 Bae JA, Moon D, Yoon JH. 2009. Nup211, the fission yeast homolog of Mlp1/Tpr, is
692 involved in mRNA export. J Microbiol. 47:337-343.
693 doi:10.1007/s12275-009-0125-7.

694 Bähler J, Wu JQ, Longtine MS, Shah NG, McKenzie A 3rd, Steever AB, Wach A,
695 Philippsen P, Pringle JR. 1998. Heterologous modules for efficient and versatile
696 PCR-based gene targeting in *Schizosaccharomyces pombe*. Yeast. 14: 943-951.
697 doi:10.1002/(SICI)1097-0061(199807)14:10<943::AID-YEA292>3.0.CO;2-Y

698 Baï SW, Rouquette J, Umeda M, Faigle W, Loew D, Sazer S, Doye V. 2004. The fission

699 yeast Nup107-120 complex functionally interacts with the small GTPase Ran/Spi1
700 and is required for mRNA export, nuclear pore distribution, and proper cell
701 division. Mol Cell Biol. 24: 6379-6392. doi:10.1128/MCB.24.14.6379-6392.2004
702 Belgareh N, Rabut G, Baï SW, van Overbeek M, Beaudouin J, Daigle N, Zatsepina OV,
703 Pasteau F, Labas V, Fromont-Racine M, Ellenberg J, Doye V. 2001. An
704 evolutionarily conserved NPC subcomplex, which redistributes in part to
705 kinetochores in mammalian cells. J Cell Biol. 154: 1147-1160.
706 doi:10.1083/jcb.200101081
707 Berke IC, Boehmer T, Blobel G, Schwartz TU. 2004. Structural and functional analysis
708 of Nup133 domains reveals modular building blocks of the nuclear pore complex.
709 J Cell Biol. 167:591-597. doi:10.1083/jcb.200408109
710 Bilokapic S, Schwartz TU. 2012. Molecular basis for Nup37 and ELY5/ELYS
711 recruitment to the nuclear pore complex. Proc Natl Acad Sci U S A. 109:
712 15241-15246. doi:10.1073/pnas.1205151109
713 Boehmer T, Enninga J, Dales S, Blobel G, Zhong H. 2003. Depletion of a single
714 nucleoporin, Nup107, prevents the assembly of a subset of nucleoporins into the
715 nuclear pore complex. Proc Natl Acad Sci U S A. 100: 981-985.
716 doi:10.1073/pnas.252749899
717 Boulanger J, Kervrann C, Bouthemy P. 2009. A simulation and estimation framework
718 for intracellular dynamics and trafficking in video-microscopy and fluorescence
719 imagery. Med. Image Anal. 13:132–142. doi:10.1016/j.media.2008.06.017.
720 Bui KH, von Appen A, DiGuilio AL, Ori A, Sparks L, Mackmull MT, Bock T, Hagen W,
721 Andrés-Pons A, Glavy JS, Beck M. 2013. Integrated structural analysis of the
722 human nuclear pore complex scaffold. Cell. 155: 1233-1243.

723 doi:10.1016/j.cell.2013.10.055
724 Chen XQ, Du X, Liu J, Balasubramanian MK, Balasundaram D. 2004. Identification of
725 genes encoding putative nucleoporins and transport factors in the fission yeast
726 *Schizosaccharomyces pombe*: a deletion analysis. Yeast. 21: 495-509.
727 doi:10.1002/yea.1115
728 Chikashige Y, Kurokawa R, Haraguchi T, Hiraoka Y. 2004. Meiosis induced by
729 inactivation of Pat1 kinase proceeds with aberrant nuclear positioning of
730 centromeres in the fission yeast *Schizosaccharomyces pomb*e. Genes Cells. 9:
731 671-684. doi:10.1111/j.1356-9597.2004.00760.x
732 Cho AR, Yang KJ, Bae Y, Bahk YY, Kim E, Lee H, Kim JK, Park W, Rhim H, Choi SY,
733 Imanaka T, Moon S, Yoon J, Yoon SK. 2009. Tissue-specific expression and
734 subcellular localization of ALADIN, the absence of which causes human triple A
735 syndrome. Exp. Mol. Med. 41: 381–386. doi:10.3858/emm.2009.41.6.043
736 Cronshaw JM, Krutchinsky AN, Zhang W, Chait BT, Matunis MJ. 2002. Proteomic
737 analysis of the mammalian nuclear pore complex. J Cell Biol. 158: 915-927.
738 doi:10.1083/jcb.200206106
739 D'Angelo MA, Anderson DJ, Richard E, Hetzer MW. 2006. Nuclear pores form de novo
740 from both sides of the nuclear envelope. Science. 312: 440-443.
741 doi:10.1126/science.1124196
742 D'Angelo MA, Raices M, Panowski SH, Hetzer MW. 2009. Age-dependent
743 deterioration of nuclear pore complexes causes a loss of nuclear integrity in
744 postmitotic cells. Cell 136: 284-295. doi:10.1016/j.cell.2008.11.037
745 D'Angelo MA, Gomez-Cavazos JS, Mei A, Lackner DH, Hetzer MW. 2012. A change in
746 nuclear pore complex composition regulates cell differentiation. Dev Cell. 22:

747 446-458. doi: 10.1016/j.devcel.2011.11.021
748 DeGrasse JA, DuBois KN, Devos D, Siegel TN, Sali A, Field MC, Rout MP, Chait BT.
749 2009. Evidence for a shared nuclear pore complex architecture that is conserved
750 from the last common eukaryotic ancestor. Mol Cell Proteomics. 8: 2119-2130.
751 doi:10.1074/mcp.M900038-MCP200
752 Doye V, Wepf R, Hurt EC. 1994. A novel nuclear pore protein Nup133p with distinct
753 roles in poly(A)+ RNA transport and nuclear pore distribution. EMBO J.
754 13:6062-6075. doi:10.1002/j.1460-2075.1994.tb06953.x
755 Eisenhardt N, Redolfi J, Antonin W. 2014. Interaction of Nup53 with Ndc1 and Nup155
756 is required for nuclear pore complex assembly. J Cell Sci. 127:908-921. doi:
757 10.1242/jcs.141739
758 Fernandez-Martinez J, Phillips J, Sekedat MD, Diaz-Avalos R, Velazquez-Muriel J,
759 Franke JD, Williams R, Stokes DL, Chait BT, Sali A, Rout MP. 2012.
760 Structure-function mapping of a heptameric module in the nuclear pore complex.
761 J. Cell Biol. 196: 419-434. doi:10.1083/jcb.201109008
762 Flemming D, Thierbach K, Stelter P, Böttcher B, Hurt E. 2010. Precise mapping of
763 subunits in multiprotein complexes by a versatile electron microscopy label. Nat
764 Struct Mol Biol. 17: 775-778. doi:10.1038/nsmb.1811
765 Frost A, Elgort MG, Brandman O, Ives C, Collins SR, Miller-Vedam L, Weibezahn J,
766 Hein MY, Poser I, Mann M, Hyman AA, Weissman JS. 2012. Functional
767 repurposing revealed by comparing *S. pombe* and *S. cerevisiae* genetic
768 interactions. Cell. 149: 1339-1352. doi:10.1016/j.cell.2012.04.028
769 Goudreault M, D'Ambrosio LM, Kean MJ, Mullin MJ, Larsen BG, Sanchez A,
770 Chaudhry S, Chen GI, Sicheri F, Nesvizhskii AI, Aebersold R, Raught B, Gingras

771 AC. 2009. A PP2A phosphatase high density interaction network identifies a novel
772 striatin-interacting phosphatase and kinase complex linked to the cerebral
773 cavernous malformation 3 (CCM3) protein. Molecular & Cellular Proteomics.
774 8:157-171. doi:10.1074/mcp.M800266-MCP200
775 Griffis ER, Xu S, Powers MA. 2003. Nup98 localizes to both nuclear and cytoplasmic
776 sides of the nuclear pore and binds to two distinct nucleoporin subcomplexes. Mol
777 Biol Cell. 14: 600-610. doi:10.1091/mbc.E02-09-0582
778 Hakhverdyan Z, Domanski M, Hough LE, Oroskar AA, Oroskar AR, Keegan S,
779 Dilworth DJ, Molloy KR, Sherman V, Aitchison JD, Fenyö D, Chait BT, Jensen
780 TH, Rout MP, LaCava J. 2015. Rapid, optimized interactomic screening. Nat
781 Methods. 12: 553-560. doi: 10.1038/nmeth.3395.
782 Harel A, Orjalo AV, Vincent T, Lachish-Zalait A, Vasu S, Shah S, Zimmerman E,
783 Elbaum M, Forbes DJ. 2003. Removal of a single pore subcomplex results in
784 vertebrate nuclei devoid of nuclear pores. Mol Cell. 11: 853-864.
785 doi:10.1016/S1097-2765(03)00116-3
786 Hodel AE, Hodel MR, Griffis ER, Hennig KA, Ratner GA, Xu S, Powers MA. 2002.
787 The three-dimensional structure of the autoproteolytic, nuclear pore-targeting
788 domain of the human nucleoporin Nup98. Mol Cell. 10: 347-358.
789 doi:10.1016/S1097-2765(02)00589-0
790 Iwamoto M, Asakawa H, Ohtsuki C, Osakada H, Koujin T, Hiraoka Y, Haraguchi T.
791 2013. Monoclonal antibodies recognize Gly-Leu-Phe-Gly repeat of nucleoporin
792 Nup98 of *Tetrahymena*, yeasts, and humans. Monoclon Antib Immunodiagn
793 Immunother. 32: 81-90. doi: 10.1089/mab.2012.0118
794 Iwamoto M, Osakada H, Mori C, Fukuda Y, Nagao K, Obuse C, Hiraoka Y, Haraguchi T.

795 2017. Compositionally distinct nuclear pore complexes of functionally distinct
796 dimorphic nuclei in the ciliate *Tetrahymena*. J Cell Sci. 130: 1822-1834.
797 doi:10.1242/jcs.199398
798 Kampmann M, Blobel G. 2009. Three-dimensional structure and flexibility of a
799 membrane-coating module of the nuclear pore complex. Nat Struct Mol Biol. 16:
800 782-788. doi:10.1038/nsmb.1618
801 Karrer KM. 2012. Nuclear dualism. Methods Cell Biol. 109: 29-52.
802 doi:10.1016/B978-0-12-385967-9.00003-7
803 Kelley K, Knockenhauer KE, Kabachinski G, Schwartz TU. 2015. Atomic structure of
804 the Y complex of the nuclear pore. Nat Struct Mol Biol. 22: 425-431.
805 doi:10.1038/nsmb.2998
806 Kim SJ, Fernandez-Martinez J, Nudelman I, Shi Y, Zhang W, Raveh B, Herricks T,
807 Slaughter BD, Hogan JA, Upla P, Chemmama IE, Pellarin R, Echeverria I,
808 Shivaraju M, Chaudhury AS, Wang J, Williams R, Unruh JR, Greenberg CH,
809 Jacobs EY, Yu Z, de la Cruz MJ, Mironska R, Stokes DL, Aitchison JD, Jarrold
810 MF, Gerton JL, Ludtke SJ, Akey CW, Chait BT, Sali A, Rout MP. 2018.
811 Integrative structure and functional anatomy of a nuclear pore complex. Nature.
812 555:475-482. doi:10.1038/nature26003.
813 Knockenhauer KE, Schwartz TU. 2016. The nuclear pore complex as a flexible and
814 dynamic gate. Cell. 164: 1162-1171. doi:10.1016/j.cell.2016.01.034
815 Kosinski J, Mosalaganti S, von Appen A, Teimer R, DiGuilio AL, Wan W, Bui KH,
816 Hagen WJ, Briggs JA, Glavy JS, Hurt E, Beck M. 2016. Molecular architecture of
817 the inner ring scaffold of the human nuclear pore complex. Science. 352: 363-365.
818 doi: 10.1126/science.aaf0643

819 Krull S, Thyberg J, Björkroth B, Rackwitz HR, Cordes VC. 2004. Nucleoporins as
820 components of the nuclear pore complex core structure and Tpr as the
821 architectural element of the nuclear basket. Mol Biol Cell. 15:4261-4277.
822 doi:10.1091/mbc.e04-03-0165
823 Lin DH, Stuwe T, Schilbach S, Rundlet EJ, Perriches T, Mobbs G, Fan Y, Thierbach K,
824 Huber FM, Collins LN, Davenport AM, Jeon YE, Hoelz A. 2016. Architecture of
825 the symmetric core of the nuclear pore. Science. 352, aaf1015.
826 doi:10.1126/science.aaf1015
827 Liu HL, De Souza CP, Osmani AH, Osmani SA. 2009. The three fungal transmembrane
828 nuclear pore complex proteins of *Aspergillus nidulans* are dispensable in the
829 presence of an intact An-Nup84-120 complex. Mol. Biol. Cell. 20: 616-630.
830 doi:10.1091/mbc.E08-06-0628.
831 Liu NN, Han TX, Du LL, Zhou JQ. 2010. A genome-wide screen for
832 *Schizosaccharomyces pombe* deletion mutants that affect telomere length. Cell
833 Res. 20: 963-965. doi:10.1038/cr.2010.107
834 Loïodice I, Alves A, Rabut G, Van Overbeek M, Ellenberg J, Sibarita JB, Doye V. 2004.
835 The entire Nup107-160 complex, including three new members, is targeted as one
836 entity to kinetochores in mitosis. Mol Biol Cell. 15: 3333-3344.
837 doi:10.1091/mbc.E03-12-0878
838 Lutzmann M, Kunze R, Buerer A, Aebi U, Hurt E. 2002. Modular self-assembly of a
839 Y-shaped multiprotein complex from seven nucleoporins. EMBO J. 21: 387-397.
840 doi:10.1093/emboj/21.3.387
841 Maimon T, Elad N, Dahan I, Medalia O. 2012. The human nuclear pore complex as
842 revealed by cryo-electron tomography. Structure. 20: 998-1006. doi:

843 10.1016/j.str.2012.03.025.
844 Matsuda A. 2018. Chromagnon. Github. https://github.com/macronucleus/chromagnon.
845 84d4506.
846 Matsuda A, Shao L, Boulanger J, Kervrann C, Carlton PM, Kner P, Agard D, Sedata JW.
847 2010. Condensed mitotic chromosome structure at nanometer resolution using
848 PALM and EGFP- histones. PLoS ONE 5: e12768.
849 Matsuda A, Schermelleh L, Hirano Y, Haraguchi T, Hiraoka Y. 2018. Accurate and
850 fiducial-marker-free correction for three-dimensional chromatic shift in biological
851 fluorescence microscopy. Sci Rep. 8:7583. doi:10.1038/s41598-018-25922-7.
852 Mishra RK, Chakraborty P, Arnaoutov A, Fontoura BM, Dasso M. 2010. The
853 Nup107-160 complex and gamma-TuRC regulate microtubule polymerization at
854 kinetochores. Nat Cell Biol. 12: 164-169. doi:10.1038/ncb2016
855 Moreno S, Klar A, Nurse P. 1991. Molecular genetic analysis of fission yeast
856 *Schizosaccharomyces pombe*. Methods Enzymol. 194: 795-823.
857 doi:10.1016/0076-6879(91)94059-L
858 Moreno CS, Lane WS, Pallas DC. 2001. A mammalian homolog of yeast MOB1 is both
859 a member and a putative substrate of striatin family-protein phosphatase 2A
860 complexes. J. Biol. Chem. 276: 24253–24260. doi:10.1074/jbc.M102398200
861 Mosalaganti S, Kosinski J, Albert S, Schaffer M, Strenkert D, Salomé PA, Merchant SS,
862 Plitzko JM, Baumeister W, Engel BD, Beck M. 2018. In situ architecture of the
863 algal nuclear pore complex. Nature Comm. 9: 236.
864 doi :10.1038/s41467-018-04739-y
865 Nie M, Boddy MN. 2015. Pli1(PIAS1) SUMO ligase protected by the nuclear
866 pore-associated SUMO protease Ulp1SENP1/2. J Biol Chem. 290: 22678-22685.

867 doi:10.1074/jbc.M115.673038
868 Nozawa RS, Nagao K, Igami KT, Shibata S, Shirai N, Nozaki N, Sado T, Kimura H,
869 Obuse C. 2013. Human inactive X chromosome is compacted through a
870 polycomb-independent SMCHD1-HBiX1 pathway. Nature Structure & Molecular
871 Biology 20: 566–573. doi:10.1038/nsmb.2532
872 Obado SO, Brillantes M, Uryu K, Zhang W, Ketaren NE, Chait BT, Field MC, Rout MP.
873 2016a. Interactome mapping reveals the evolutionary history of the nuclear pore
874 complex. PLoS Biol. 14: e1002365. doi:10.1371/journal.pbio.1002365
875 Obado SO, Field MC, Chait BT, Rout MP. 2016b. High-efficiency isolation of nuclear
876 envelope protein complexes from Trypanosomes. Methods Mol Biol. 1411: 67-80.
877 doi: 10.1007/978-1-4939-3530-7_3.
878 Olsson M, Schéele S, Ekblom P. 2004. Limited expression of nuclear pore membrane
879 glycoprotein 210 in cell lines and tissues suggests cell-type specific nuclear pores
880 in metazoans. Exp Cell Res. 292, 359-370. doi:10.1016/j.yexcr.2003.09.014
881 Onischenko E, Stanton LH, Madrid AS, Kieselbach T, Weis K. 2009. Role of the Ndc1
882 interaction network in yeast nuclear pore complex assembly and maintenance. J
883 Cell Biol. 185:475-491. doi: 10.1083/jcb.200810030
884 Ori A, Banterle N, Iskar M, Andrés-Pons A, Escher C, Bui KH, Sparks L,
885 Solis-Mezarino V, Rinner O, Bork P, Lemke EA, Beck M. 2013. Cell type-specific
886 nuclear pores: a case in point for context-dependent stoichiometry of molecular
887 machines. Mol Syst Biol. 9: 648. doi:10.1038/msb.2013.4
888 Orjalo AV, Arnaoutov A, Shen Z, Boyarchuk Y, Zeitlin SG, Fontoura B, Briggs S, Dasso
889 M, Forbes DJ. 2006. The Nup107-160 nucleoporin complex is required for correct
890 bipolar spindle assembly. Mol Biol Cell. 17: 3806-3818.

891 doi:10.1091/mbc.E05-11-1061
892 Platani M, Santarella-Mellwig R, Posch M, Walczak R, Swedlow JR, Mattaj IW. 2009.
893 The Nup107-160 nucleoporin complex promotes mitotic events via control of the
894 localization state of the chromosome passenger complex. Mol Biol Cell. 20:
895 5260-5275. doi:10.1091/mbc.E09-05-0377
896 Raices M, D'Angelo MA. 2012. Nuclear pore complex composition: a new regulator of
897 tissue-specific and developmental functions. Nat Rev Mol Cell Biol. 13: 687-699.
898 doi:10.1038/nrm3461
899 Rasala BA, Orjalo AV, Shen Z, Briggs S, Forbes DJ. 2006. ELYS is a dual
900 nucleoporin/kinetochore protein required for nuclear pore assembly and proper
901 cell division. Proc Natl Acad Sci U S A. 103: 17801-17806.
902 doi:10.1073/pnas.0608484103
903 Ratner GA, Hodel AE, Powers MA.2007. Molecular determinants of binding between
904 Gly-Leu-Phe-Gly nucleoporins and the nuclear pore complex. J Biol Chem. 282:
905 33968-33976. doi:10.1074/jbc.M707911200
906 Rout MP, Aitchison JD, Suprapto A, Hjertaas K, Zhao Y, Chait BT. 2000. The yeast
907 nuclear pore complex: composition, architecture, and transport mechanism. J Cell
908 Biol. 148: 635-651. doi:10.1083/jcb.148.4.635
909 Saitoh S, Takahashi K, Yanagida M. 1997. Mis6, a fission yeast inner centromere
910 protein, acts during G1/S and forms specialized chromatin required for equal
911 segregation. Cell. 90: 131-143. doi:10.1016/S0092-8674(00)80320-7
912 Salas-Pino S, Gallardo P, Barrales RR, Braun S, Daga RR. 2017. The fission yeast
913 nucleoporin Alm1 is required for proteasomal degradation of kinetochore
914 components. J Cell Biol. 216:3591-3608. doi:10.1083/jcb.201612194.

915 Sawin KE, Nurse P. 1997. Photoactivation of green fluorescent protein. Curr Biol 7:
916 R606-607
917 Singh NS, Shao N, McLean JR, Sevugan M, Ren L, Chew TG, Bimbo A, Sharma R,
918 Tang X, Gould KL, Balasubramanian MK. 2011. SIN-inhibitory phosphatase
919 complex promotes Cdc11p dephosphorylation and propagates SIN asymmetry in
920 fission yeast. Curr Biol. 21: 1968-1978. doi:10.1016/j.cub.2011.10.051
921 Strambio-de-Castillia C, Blobel G, Rout MP. 1999. Proteins connecting the nuclear pore
922 complex with the nuclear interior. J Cell Biol. 144:839-855.
923 doi:10.1083/jcb.144.5.839
924 Stuwe T, von Borzyskowski LS, Davenport AM, Hoelz A. 2012. Molecular basis for the
925 anchoring of proto-oncoprotein Nup98 to the cytoplasmic face of the nuclear pore
926 complex. J Mol Biol. 419: 330-346. doi:10.1016/j.jmb.2012.03.024
927 Stuwe T, Correia AR, Lin DH, Paduch M, Lu VT, Kossiakoff AA, Hoelz A. 2015.
928 Nuclear pores. Architecture of the nuclear pore complex coat. Science. 347:
929 1148-1152. doi:10.1126/science.aaa4136
930 Tamura K, Fukao Y, Iwamoto M, Haraguchi T, Hara-Nishimura I. 2010. Identification
931 and characterization of nuclear pore complex components in *Arabidopsis thaliana*.
932 Plant Cell. 22: 4084-4097. doi:10.1105/tpc.110.079947
933 Thierbach K, von Appen A, Thoms M, Beck M, Flemming D, Hurt E. 2013. Protein
934 interfaces of the conserved Nup84 complex from *Chaetomium thermophilum*
935 shown by crosslinking mass spectrometry and electron microscopy. Structure. 21:
936 1672-1682. doi:10.1016/j.str.2013.07.004
937 von Appen A, Kosinski J, Sparks L, Ori A, DiGuilio AL, Vollmer B, Mackmull MT,
938 Banterle N, Parca L, Kastritis P, Buczak K, Mosalaganti S, Hagen W, Andres-Pons

939 A, Lemke EA, Bork P, Antonin W, Glavy JS, Bui KH, Beck M. 2015. *In situ*
940 structural analysis of the human nuclear pore complex. Nature. 526: 140-143.
941 doi:10.1038/nature15381
942 Walther TC, Alves A, Pickersgill H, Loïodice I, Hetzer M, Galy V, Hülsmann BB,
943 Köcher T, Wilm M, Allen T, Mattaj IW, Doye V. 2003. The conserved
944 Nup107-160 complex is critical for nuclear pore complex assembly. Cell. 113:
945 195-206. doi:10.1016/S0092-8674(03)00235-6
946 Whittle JR, Schwartz TU. 2009. Architectural nucleoporins Nup157/170 and Nup133
947 are structurally related and descend from a second ancestral element. J Biol Chem.
948 284: 28442-28452. doi:10.1074/jbc.M109.023580
949 Yang HJ, Asakawa H, Haraguchi T, Hiraoka Y. 2015. Nup132 modulates meiotic
950 spindle attachment in fission yeast by regulating kinetochore assembly. J Cell Biol.
951 211: 295-308. doi:10.1083/jcb.201501035
952 Zuccolo M, Alves A, Galy V, Bolhy S, Formstecher E, Racine V, Sibarita JB, Fukagawa
953 T, Shiekhattar R, Yen T, Doye V. 2007. The human Nup107-160 nuclear pore
954 subcomplex contributes to proper kinetochore functions. EMBO J. 26: 1853-1864.
955 doi:10.1038/sj.emboj.7601642
956

Figures with legends

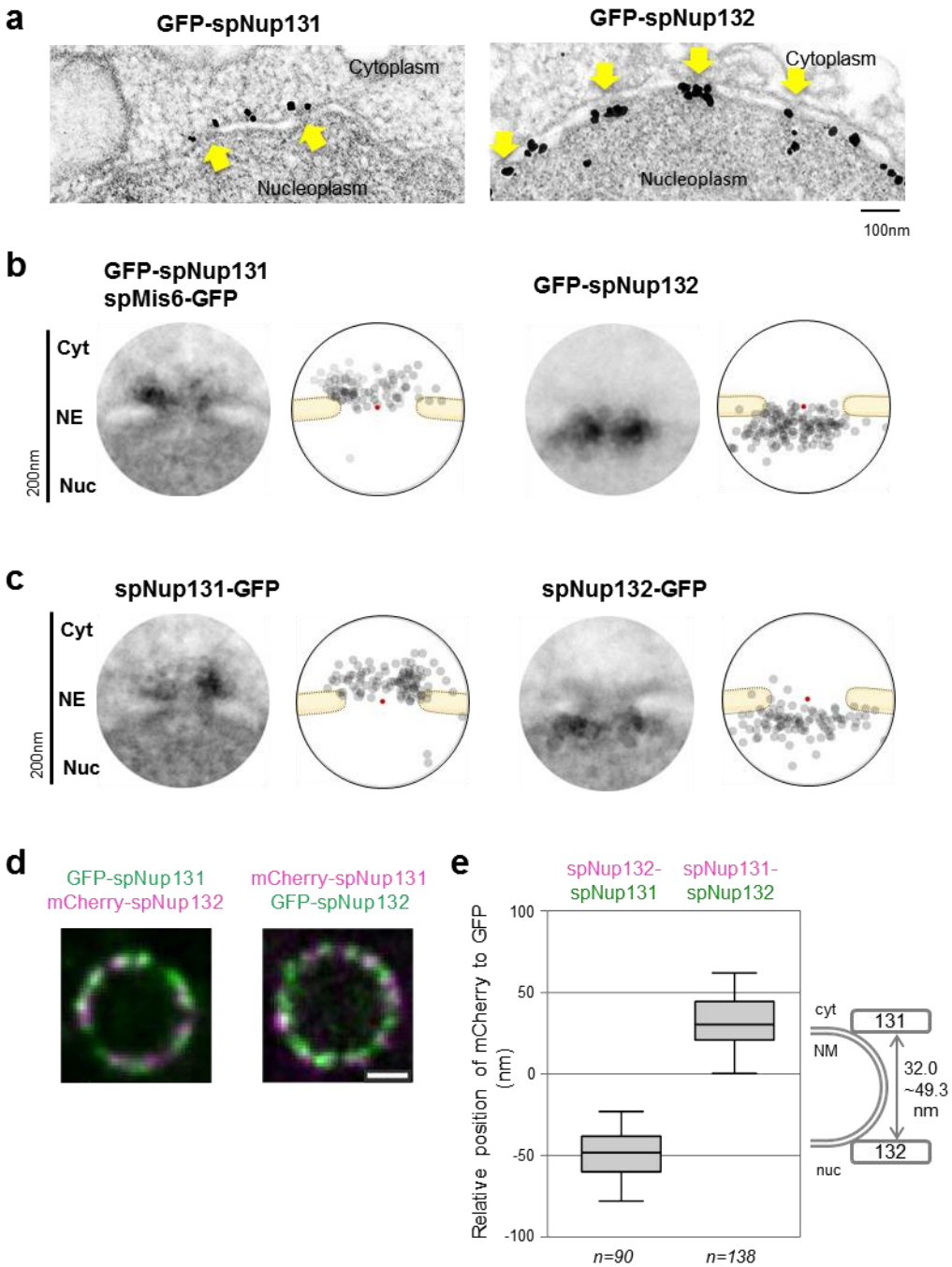

Fig. 1 Localization of spNup131 and spNup132 at the NPC. **a** IEM of GFP-spNup131 and GFP-spNup132. Arrows indicate the nuclear pores. Scale bar, 100 nm. **b** Quantitative representation of IEM for N-terminally tagged spNup131 and spNup132. (left) A montage image of 20 immunoelectron micrographs. The diameter of the circle is 200 nm. (right) A schematic drawing illustrating the distribution of immunogold

particles shown in the montage image. Red dots represent the pore centers. **c** Quantitative representation of IEM for C-terminally tagged spNup131 and spNup132. Montage pictures and distributions of immunogold particles are shown as described in **b**. IEM micrographs used for the quantitative analysis are available in Figure 1—source data 1. **d** Fluorescence microscopy of a nucleus simultaneously expressing spNup131 and spNup132 fused to GFP and mCherry in living cells. (left) A nucleus expressing GFP-spNup131 and mCherry-spNup132. Green, GFP-spNup131; Magenta, mCherry-spNup132. (right) A nucleus expressing mCherry-spNup131 and GFP-spNup132. Magenta, mCherry-spNup132; Green, GFP-spNup131. Scale bar, 1 μm. **e** Distances between spNup131 and spNup132 in living cells. Results from cells expressing GFP-spNup131 and mCherry-spNup132 (n=90, left) and results from cells expressing mCherry-spNup131 and GFP-spNup132 (n=138, right) are shown in the box plot: values of the distance determined in individual cells are shown in Figure 1—source data 2. Center lines show the medians; box limits indicate the 25th and 75th percentiles. Whiskers extend to the 5th and 95th percentiles. The diagram on the right shows the positions of spNup131 and spNup132 within the NPC.

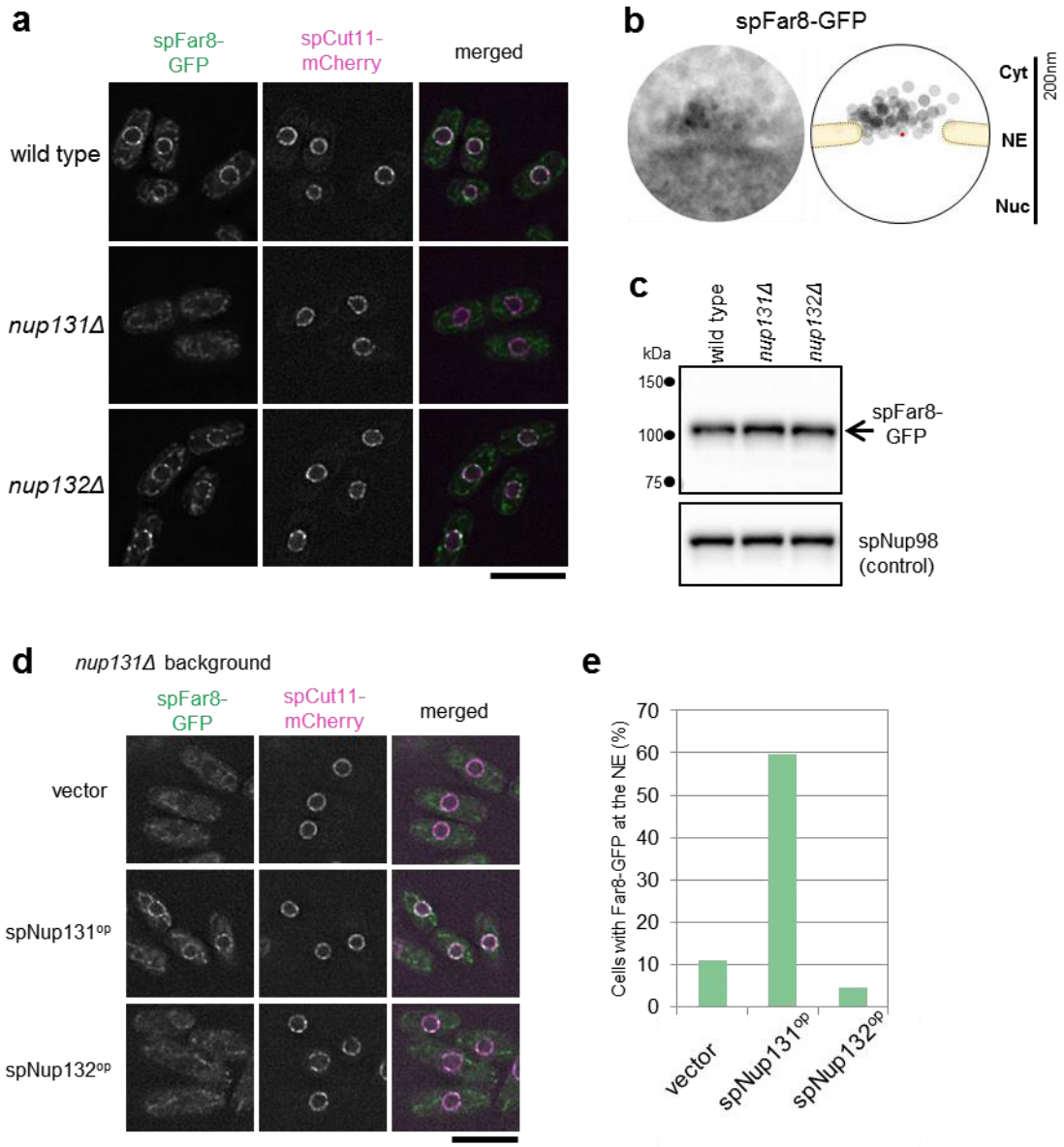

Fig. 2 spNup131 is required for spFar8 localization on the cytoplasmic side of the NPC. **a** Localization of spFar8-GFP in wild type, *nup131*Δ, and *nup132*Δ cells. spFar8-GFP was expressed in the indicated strains, and cells exponentially growing in EMM2 liquid medium were observed by FM. spCut11-mCherry was observed as an NPC marker. Scale bar, 10 μm. **b** IEM of spFar8-GFP. For quantitative representation, a montage image of 20 immunoelectron micrographs and a schematic drawing illustrating the distribution of immunogold particles are shown. The red point indicates the pore center.

IEM micrographs used for the quantitative analysis are available in Figure 2—source data 3. **c** Western blot analysis of spFar8-GFP. Whole cell extracts were prepared from wild type, *nup131*Δ, and *nup132*Δ cells expressing spFar8-GFP and subjected to SDS-PAGE and Western blot analysis. spFar8-GFP was detected with anti-GFP antibody. spNup98 was detected with anti-Nup98 antibody (13C2) as a loading control. The arrow indicates the position of spFar8-GFP. Small dots on the left indicate positions of molecular weight markers. **d** Overexpression of spNup131 and spNup132 in *nup131*Δ cells expressing spFar8-GFP. spNup131 or spNup132 were overexpressed in *nup131*Δ cells and localization of spFar8-GFP and spCut11-mCherry was observed by FM. Empty vector was also introduced for a control strain. Scale bar, 10μm. **(e)** Quantitative analysis of cells exhibiting spFar8-GFP at the NE in the experiment described in **d**. Cells observed were: 81, 102, and 130 for vector, spNup131^{op}, and spNup132^{op}, respectively.

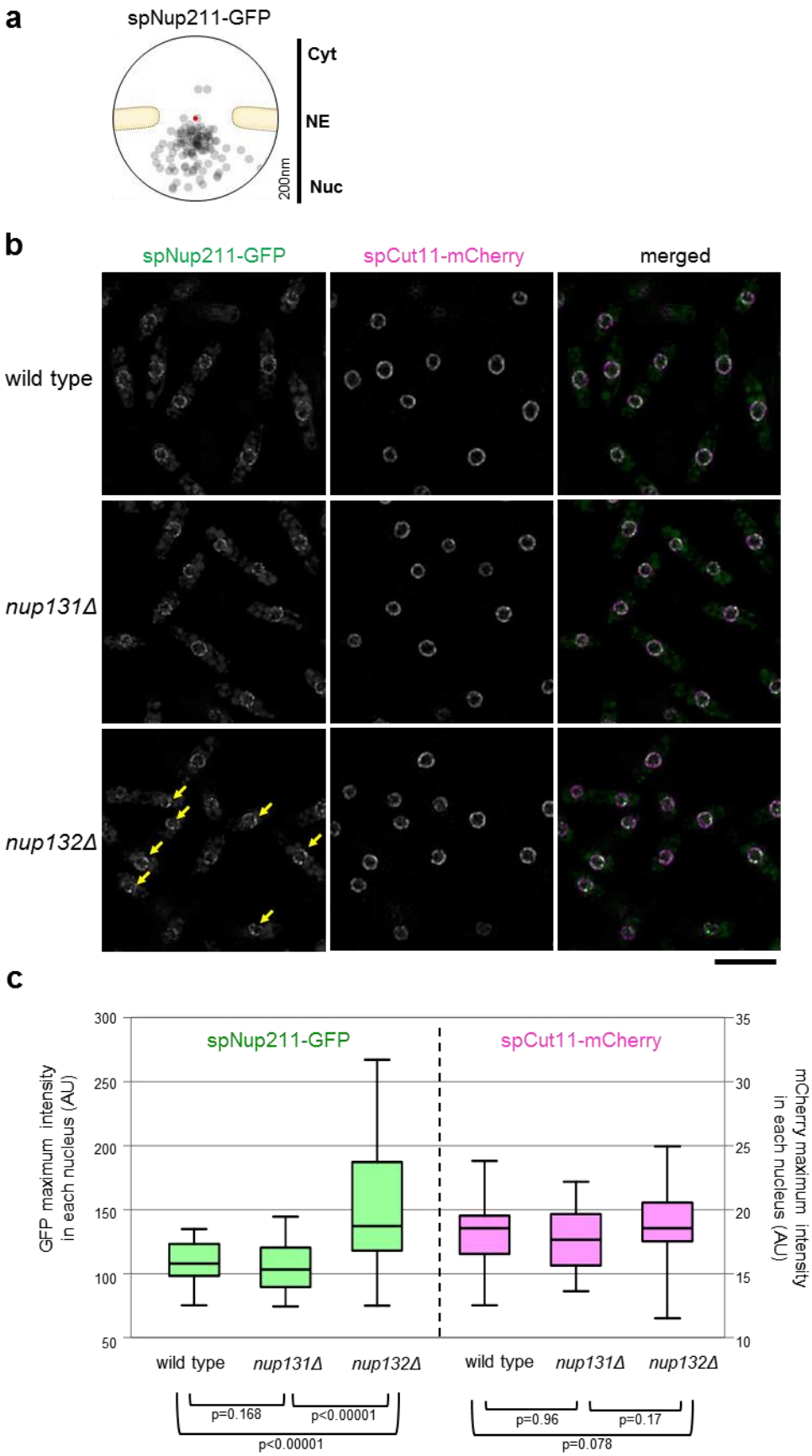
a
spNup211-GFP
Cyt
NE
Nuc
200nm
b
spNup211-GFP
spCut11-mCherry
merged
wild type
nup131Δ
nup132Δ
c
spNup211-GFP
spCut11-mCherry
GFP maximum intensity in each nucleus (AU)
mCherry maximum intensity in each nucleus (AU)
300
250
200
150
100
50
35
30
25
20
15
10
wild type
nup131Δ
nup132Δ
wild type
nup131Δ
nup132Δ
p=0.168
p<0.00001
p<0.00001
p=0.96
p=0.17
p=0.078

Fig. 3 spNup132 is required for the distribution of the nucleoplasmic nucleoporin spNup211 at the NPC. **a** IEM of spNup211-GFP. For quantitative representation, a schematic drawing illustrating the distribution of immunogold particles based on 20 immunoelectron micrographs is shown. The red point indicates the pore center. IEM micrographs used for the quantitative analysis are available in Figure 3—source data 1. **b** FM of spNup211-GFP in living cells. Arrows indicate bright dots observed in *nup132*Δ cells. Scale bar, 10 μm. **c** Maximum intensity values of spNup211-GFP and spCut11-mCherry in wild-type (n=76), *nup131*Δ (n=50), and *nup132*Δ (n=73) cells: values of the maximum intensity determined in individual cells are shown in Figure 3—source data 2. In the box plot, the center lines show the medians; box limits indicate the 25th and 75th percentiles. Whiskers extend to the 5th and 95th percentiles. Averages (±standard deviations) are 110.1±22.7, 105.0±21.5 and 154.7±64.1 for spNup211-GFP, and 18.0±3.2, 17.6±3.0 and 18.8±4.0 for spCut11-mCherry in wild-type, *nup131*Δ, and *nup132*Δ, respectively. *p* values shown at the bottom are calculated by the U-test.

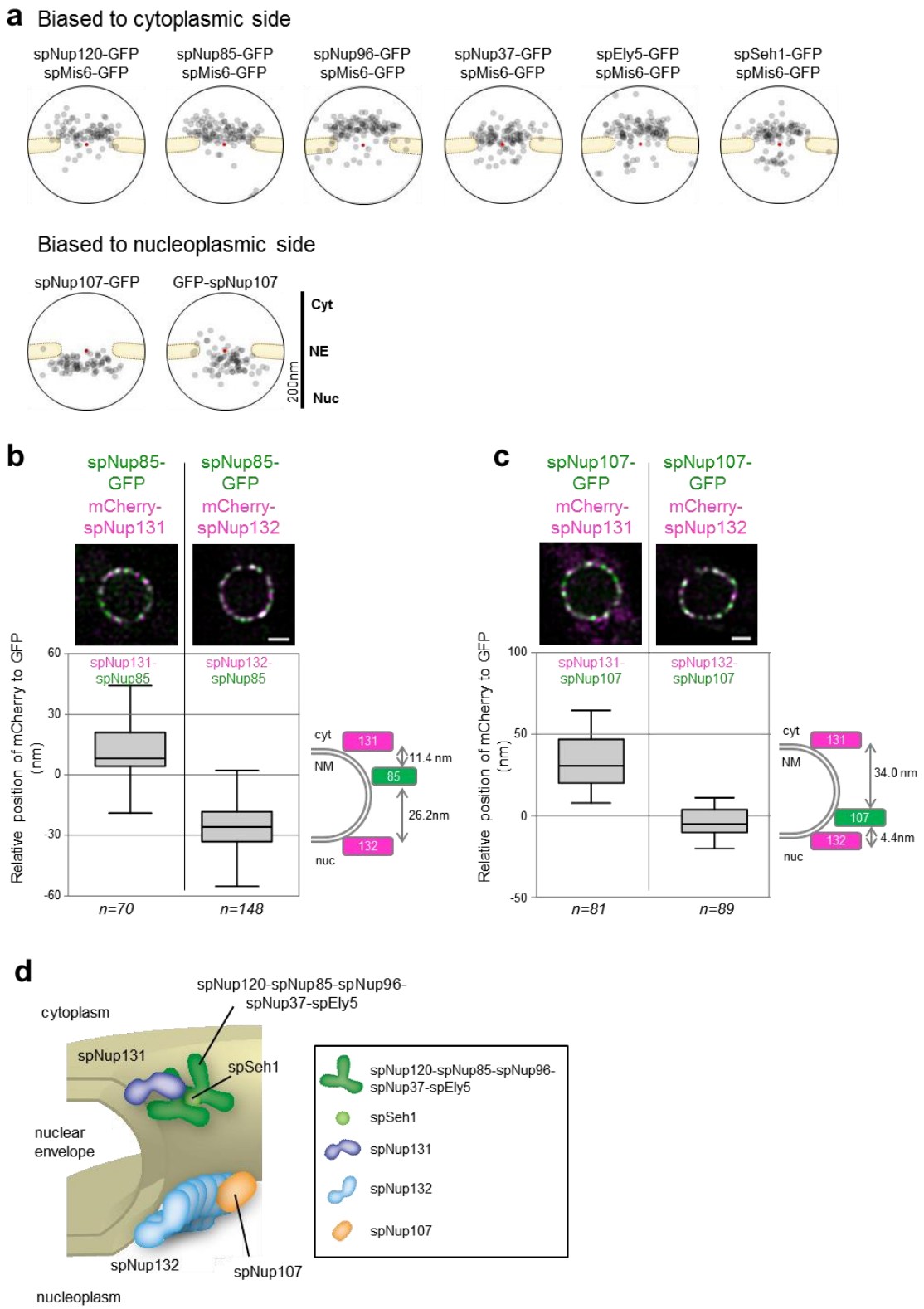

Fig. 4 Localization of Nup107-160 subcomplex orthologs. **a** IEM of *S. pombe* Nup107-160 subcomplex orthologs. Immunogold distributions of the projected

immunoelectron micrographs are shown as a quantitative representation. To confirm the accessibility of the nucleus to immunogold particles, spMis6-GFP was used. spMis6-positive nuclei were evaluated for staining with anti-GFP antibody. IEM micrographs used for the quantitative analysis are available in Figure 4—source data 1. **b** Position of spNup85-GFP determined by high-precision distance measurements using FM. **(upper panel)** FM images of a nucleus expressing spNup85-GFP and mCherry-spNup131 or mCherry–spNup132. Green, spNup85-GFP; magenta, mCherry-spNup131 or mCherry-spNup132. Scale bar, 1 μm. **(lower panel)** Distance between spNup85-GFP and mCherry-spNup131 (left) or mCherry-spNup132 (right). The relative positions of spNup131 and spNup132 to spNup85 are shown in the box plot: center lines show the medians; box limits indicate the 25th and 75th percentiles; whiskers extend to the 5th and 95th percentiles. n, cell number examined. Values of the distance determined in individual cells are shown in Figure 4—source data 2. The diagram on the right shows the positions of spNup85, spNup131 and spNup132 within the NPC. **c** Position of spNup107-GFP determined by high-precision distance measurements using FM. **(upper panel)** FM images of a nucleus expressing spNup107-GFP and mCherry-spNup131 or mCherry–spNup132. Green, spNup107-GFP; magenta, mCherry-spNup131 or mCherry-spNup132. Scale bar, 1 μm. **(lower panel)** Distance between spNup107-GFP and mCherry-spNup131 (left) or mCherry-spNup132 (right). The relative positions of spNup131 and spNup132 to spNup107 are shown in the box plot as described in **b**. Values of the distance determined in individual cells are shown in Figure 4—source data 3. The diagram on the right shows the positions of spNup107, spNup131 and spNup132 within the NPC. **d** A schematic drawing showing the localization of Nup107-160 subcomplex orthologs in *S. pombe*.

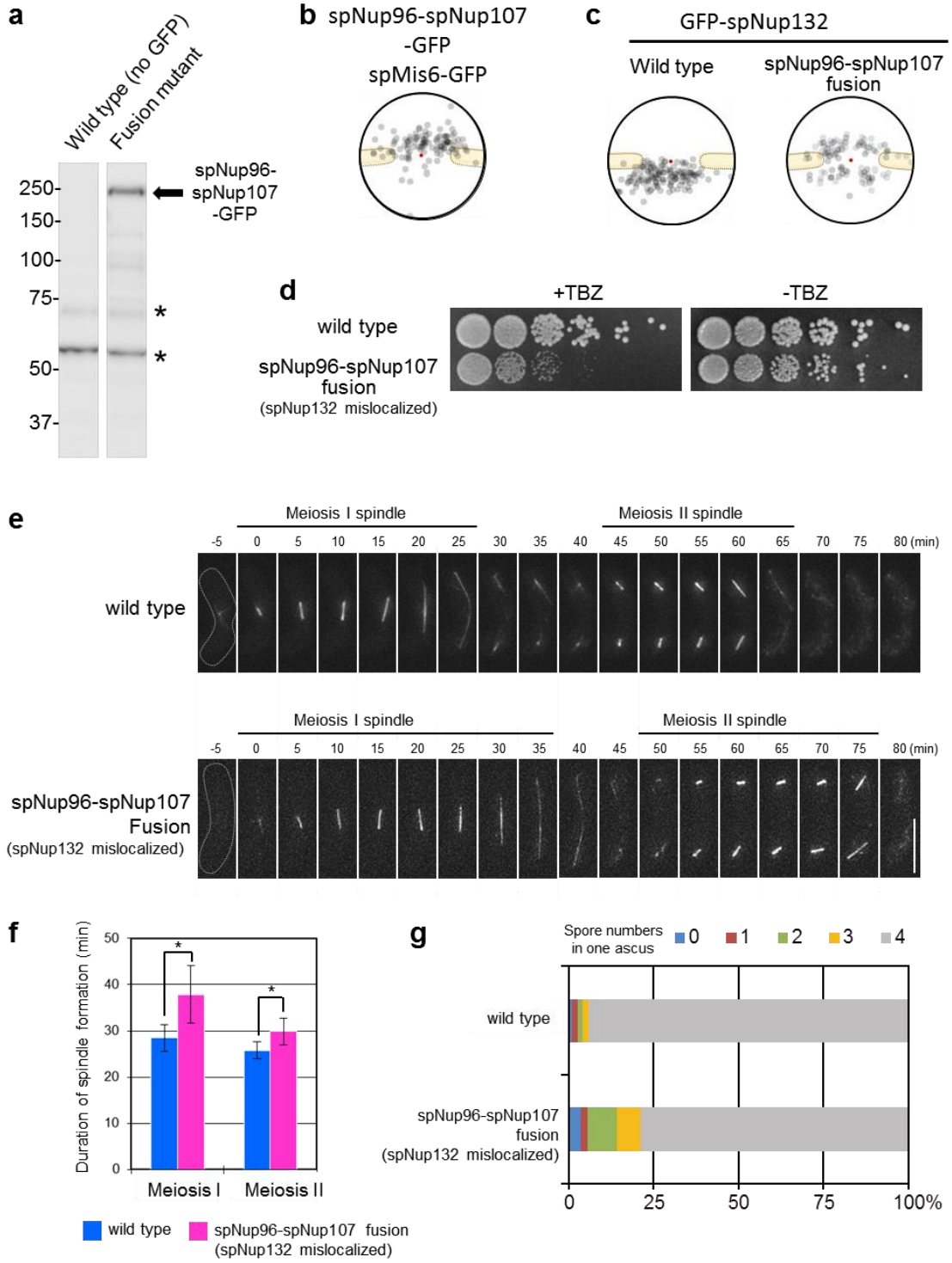

Fig. 5 Localization and functional analysis of an spNup96-spNup107 fusion Nup. **a** Western blot analysis of the spNup96-spNup107-GFP fusion protein. Asterisks represent non-specific cross reactions of the anti-GFP antibody. **b** IEM of the spNup96-spNup107 fusion protein. Immunogold distribution of the projected immunoelectron micrographs is shown. IEM micrographs used for the quantitative

analysis are available in Figure 5—source data 1. **c** IEM of GFP-spNup132 in wild type and spNup96-spNup107 fusion backgrounds. Localization of GFP-spNup132 in a wild type background is taken from the data shown in **Fig. 1b**. IEM micrographs used for the quantitative analysis are available in Figure 5—source data 1. **d** A cell growth assay in the presence (+TBZ) or absence (-TBZ) of TBZ. Five-fold serial dilutions of wild type and spNup96-spNup107 fusion strains were spotted on YES medium containing or lacking TBZ and incubated for 3 days. **e** Time-lapse observation of *S. pombe* cells (wt or spNup96-spNup107 fusion strains) undergoing meiosis. Cells expressing mCherry-fused α-tubulin (spAtb2) were induced to enter meiosis. The duration of meiosis I and II was determined as the time the spindle was present. Dotted lines show cell shapes. The time 0 indicates the time of the first appearance of meiosis I spindle formation. Representative images are shown (number of cells observed: 32 for wild type and 33 for spNup96-spNup107). **f** Statistical analysis for images obtained in **(e)**. Duration of meiosis I and II. Error bars represent standard deviations. The duration of meiosis I was 28.4 ± 3.0 min in wild type and 37.9 ± 6.3 min in spNup96-spNup107 fusion cells. The duration of meiosis II was 25.8 ± 1.8 min in wild type and 29.8 ± 2.9 min in spNup96-spNup107 fusion cells. Asterisks indicate statistical significance ($p < 0.0001$) between the indicated strains by Welch's t-test. Number of cells observed: 32 for wild type and 33 for spNup96-spNup107. **g** Abnormal spore formation was observed in the spNup96-spNup107 fusion background. More than 200 asci were counted for each strain.

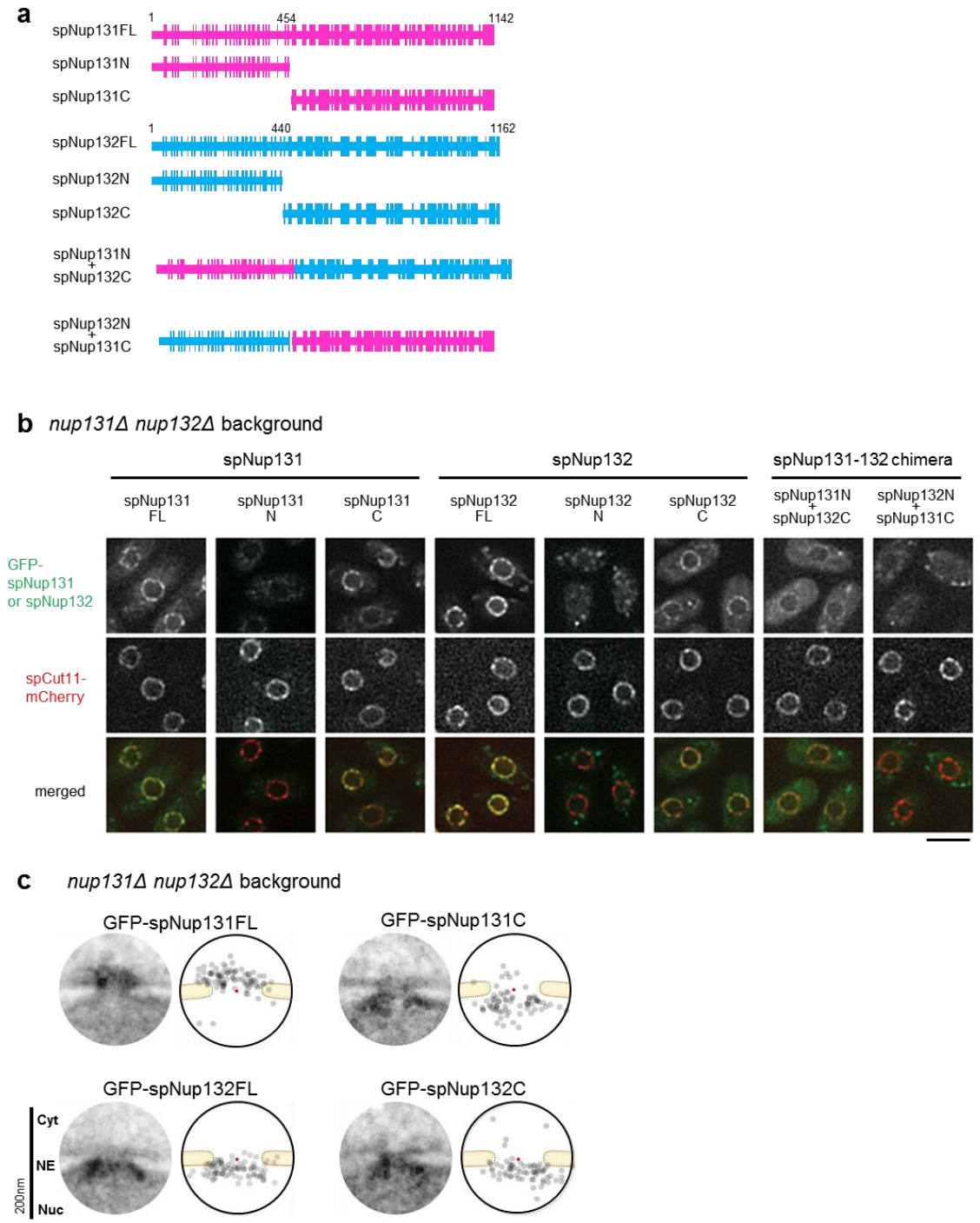

Fig. 6 Localization of the spNup131 and spNup132 domains. **a** Schematics of the spNup131 and spNup132 fragments. Magenta represents peptides from spNup131 and light blue represents peptides from spNup132. **b** Localization of spNup131 and spNup132 fragments as determined by FM. GFP-fused fragments were expressed under the spNup132 promoter in the background of the *nup131Δ nup132Δ* double mutant.

spCut11-mCherry served as an NPC marker. Scale bar, 5 μm. **c** IEM of the spNup131 and spNup132 fragments. Projection images (left) and immunogold distributions (right) are shown as described in the legend of **Fig.1b**. The red points indicate the pore centers. IEM micrographs used for the quantitative analysis are available in Figure 6—source data 1.

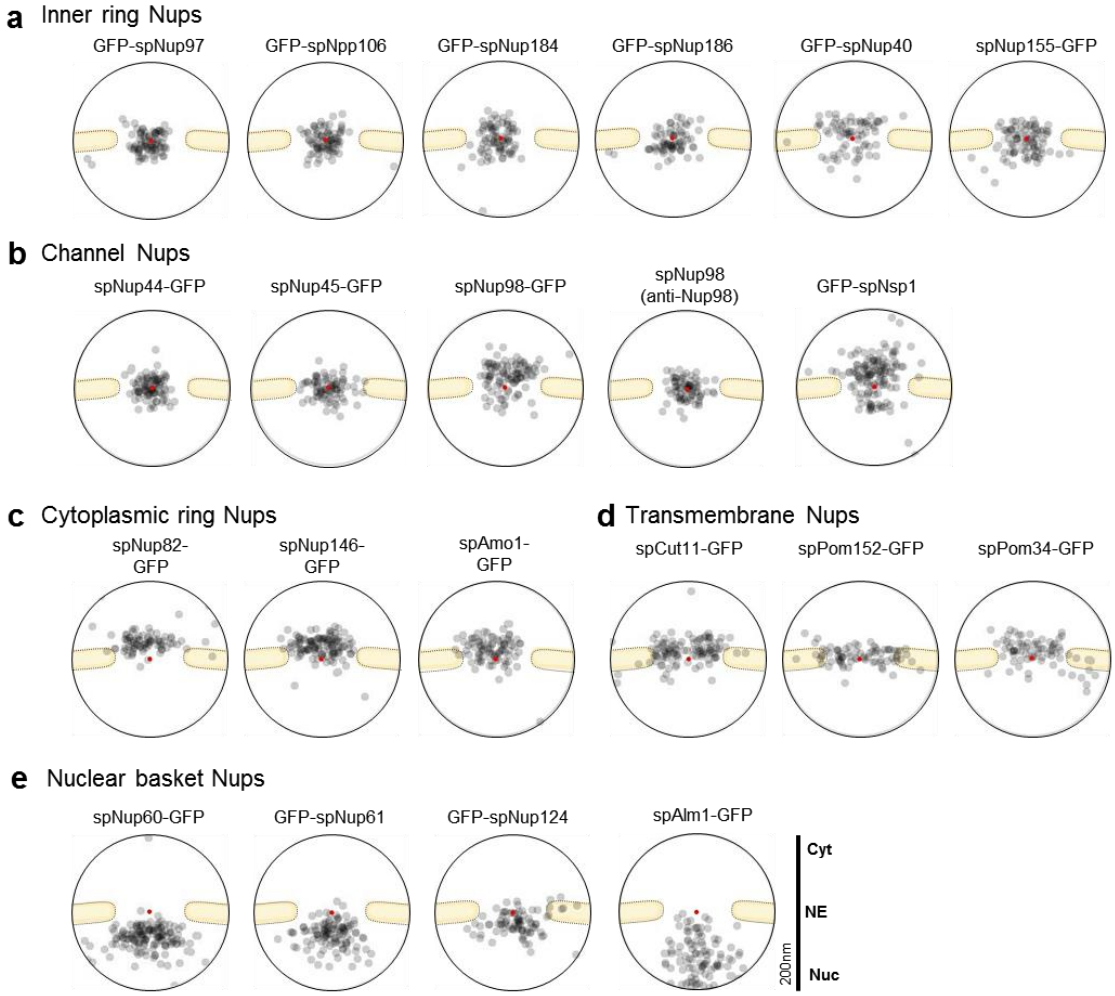

Fig. 7 IEM of *S. pombe* nucleoporins. **a** Inner ring Nups. **b** Channel Nups. IEM for spNup98 was performed using an anti-Nup98 antibody (13C2) for the wild type strain and an anti-GFP antibody for the spNup98-GFP strain. **c** Cytoplasmic ring Nups. **d** Transmembrane Nups. **e** Nuclear basket Nups. The localization of the other nuclear basket Nup, spNup211, is shown in **Figure 3a**. Immunogold distributions are shown based on the projected immunoelectron micrographs for quantitative representation. The red points indicate the pore centers. IEM micrographs used for the quantitative analysis are available in Figure 7—source data 1.

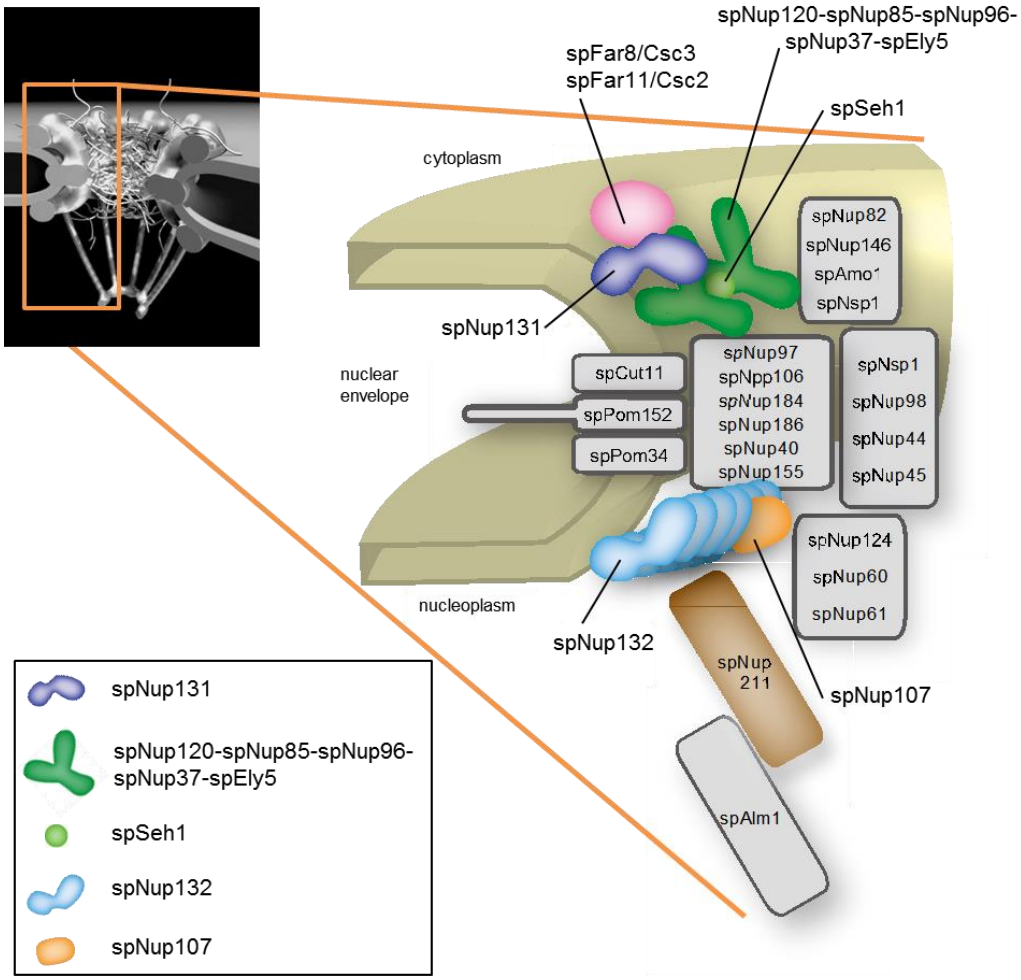

Fig. 8 Model of the *S. pombe* NPC. The positions of the *S. pombe* Nups and the relative numbers of the Nup107-160 subcomplex Nups making up a single unit of the 8-fold rotational symmetrical structure of the *S. pombe* NPC are shown. The positions of the subcomplexes were deduced based on the IEM analysis in this study. The numbers of the Nup107-160 subcomplex components were deduced based on the FM and biochemical analysis reported previously (Asakawa et al., 2014): spNup131 (1 molecule, dark blue), the spNup120-spNup85-spNup96-spNup37-spEly5 complex (2 molecules each, dark green), spSeh1 (1 molecule, light green), spNup107 (1 molecule, orange), spNup132 (6 molecules, right blue).